Aspects of Photovoltaic Systems: Study and Simulation of Silicon Phthalocyanine Bulk Heterojunction Solar Cells and Monochromatic Photonic Power Converters

Kayden Kaller

A thesis submitted to the University of Ottawa in partial fulfillment
of the requirements for the Master of Applied Science degree in
Electrical Engineering and Computer Science

School of Electrical Engineering and Computer Science
Faculty of Engineering
University of Ottawa

Abstract

This thesis discusses two different photovoltaic systems, organic solar cells, and photonic power converters. The open-source software package Solcore was used to simulate and analyze optoelectronic properties of both systems.

It is widely accepted that the transition from a fossil-fuel driven economy is necessary in the coming future. Organic solar cells are an alternative energy generation method with potential for fast energetic and economic payback periods. Bulk heterojunction organic solar cells are a common design, as they have particularly low manufacturing costs due to a simple device architecture. In this work, two bulk heterojunction blends are experimentally assessed using the acceptor molecule silicon phthalocyanine (bis(tri-*n*-butyl silyl oxide) silicon phthalocyanine ($(3BS)_2$-SiPc) as a potential low-cost non-fullerene alternative to the typical acceptor [6,6]-phenyl-C61-butyric acid methyl ester ($PC_{61}BM$). These acceptors are compared within blends with the typical donor compound poly(3-hexylthiophene) (P3HT), and also poly[(2,6-(4,8-bis(5-(2-ethylhexyl)thiophen-2-yl)-benzo [1,2-b:4,5-b']dithiophene))-alt-(5,5-(1',3'-di-2-thienyl-5',7'-bis(2-ethylhexyl)benzo[1',2'-c:4',5'-c']dithiophene-4,8-dione)] (PBDB-T). Device performance was assessed under standard conditions, increased angles of incidence, and reduced light intensities. Devices with the P3HT:$(3BS)_2$-SiPc blend achieved a power conversion efficiency (PCE) of 3.6%, which outperformed P3HT:$PC_{61}BM$ devices with a PCE of 3.0% due to a higher open-circuit voltage (V_{OC}) of 0.76 V as opposed to 0.53 V. The PBDB-T:$(3BS)_2$-SiPc achieved a high V_{OC} of 1.09 V, but had a lower PCE of 3.4% in relation to the PBDB-T:$PC_{61}BM$ device with a PCE of 6.4% and a V_{OC} of 0.78 V.

Photonic power converters are devices in optical networks that allow for optical power transmission rather than the conventional method of electrical power transmission. This provides benefits such as electrical isolation and resistance to electromagnetic interference, along with the ability to propagate along the same cable as data. These power converters are used to convert optical power to electrical power, and operate similarly to a solar cell with a narrow bandwidth. Multijunction designs are often used for increased operating voltage and efficiency. In such designs employing a vertical architecture, the bottom-most junction has the largest thickness along with the lowest efficiency due to increased recombination losses. To improve this lower efficiency, light trapping techniques can be employed to decrease the junction thickness while retaining the optical thickness. In this work, a current-matched 5-junction GaAs photonic power converter was simulated with both metallic and distributed Bragg reflectors at the rear of the device. These reflectors allowed for the thinning of the bottommost junction, which resulted in an increase in efficiency and overall power output of the power converter.

Table of Contents

i. Statement of Originality

The work presented in this thesis was performed by the author, unless otherwise noted. Research was performed under the supervision of Dr. Karin Hinzer and Dr. Benoît Lessard. To the best of the author's knowledge, all results contained in this thesis are original.

ii. Acknowledgements

Research was funded in part by the Natural Sciences and Engineering Research Council Collaborative Research and Training Experience Program (NSERC CREATE) Training in Optoelectronics for Power: From Science and Engineering to Technology grant (TOP-SET) grant number 497981,through NSERC STPGP grant 506661 number, through the University of Ottawa International Research Acceleration program, through a Government of Ontario's Ontario Graduate Scholarship (OGS), and the Electricity Human Resources Canada: Empowering Futures program.

iii. Publications and Conferences

Journal Articles

T. M. Grant, K. L. C. Kaller, T. J. Coathup, Nicole A. Rice, K. Hinzer, and B. H. Lessard, *High Voc solution-processed organic solar cells containing silicon phthalocyanine as a non-fullerene electron acceptor*, Organic Electronics. **87**, 105976 (2020).

Conferences

K. L. C. Kaller, T. J. Coathup, T. M. Grant, C. E. Valdivia, B. H. Lessard, and K. Hinzer, *Bulk heterojunction organic photovoltaic devices containing silicon phthalocyanine as a non-fullerene electron acceptor*, 2020 IEEE 47th Photovoltaic Specialists Conference, Calgary, AB, June 14-19, 2020. *Virtual poster*.

K. L. C. Kaller, C. E. Valdivia, B. H. Lessard, and K. Hinzer, *Design and modelling of photonic power converters with light management in Solcore*, 19th International Conference on Numerical Simulation of Optoelectronic Devices, Ottawa, ON, July 8 to 12, 2019. *Poster presentation*.

1 Chapter I: Introduction

1.1 Organic Solar Cells

In order to progress from a fossil-fuel driven energy economy, alternative methods of energy production need to be integrated into society. Solar power is a solution that has been actively studied over the past decades, and is desirable due to the abundant and permanent supply of solar radiation. Although solar energy represented 724 terawatt-hours (TWh) of 158,839 TWh global direct primary energy consumption in 2019 (~0.46%), it contributed 24.3% the driving force behind the 40% growth in renewable energy [1,2]. This is worth mentioning, as it is important to appreciate the sheer scale of the issue regarding the transition from fossil fuels. For example, 136,676 TWh global direct primary energy consumption (~86%) was done by coal, oil, and gas in 2019 [1,2].

Solar power is achieved through photovoltaic devices that convert sunlight into electricity. These devices contain semiconductor materials, which facilitate this energy conversion, and allow for the necessary charge transport for electricity. As of 2019, approximately 95% of photovoltaic systems produced used crystalline silicon as the semiconducting material, while other systems use thin film technologies such as cadmium telluride (CdTe), and copper indium gallium selenide (CIGS) [3]. Although these three semiconductors comprise nearly all of the solar power market, research and development is performed around the globe on other semiconducting systems. Various applications, economies, available resources, and recycling practices, among other reasons, will create advantages and disadvantages for each photovoltaic system in a given geographical location, which means that there is not a “one size fits all” solution. Additionally, since solar power represents a small percentage of current energy production, there is enough room for different technologies to flourish.

Organic solar cells (OSCs) are one such alternative, which represent a subcategory of solar cell technologies. These devices contain organic semiconducting media instead of the more conventional inorganic semiconductors, which offer certain advantages (and disadvantages), the most predominant being a decreased manufacturing cost. Instead of the highly energy demanding single crystal growth for inorganic semiconductors, organic semiconductors have the ability to be manufactured by inexpensive roll-to-roll printing techniques under atmospheric conditions, which can lead to a short energy payback time [4]. Although OSCs have a significantly shorter lifetime and a lower power conversion efficiency than inorganic cells, the short energy payback time may make these systems profitable. Researchers estimated in 2017 that the energy payback time for their OSC technology was 60 days at a lifespan of 2

years, in comparison to prototypical 1st and 2nd generation crystalline silicon systems with a payback time of <400 days and lifespan of >25 years [5]. In addition to a short energy payback time, OSCs offer other benefits such as flexibility and some transparency, which can be used for niche applications. For example, transparent OSCs can be placed on the windows of buildings with theoretical estimated energy payback times of 51 days to 1.1 years in the near future [6]. In another example, in addition to harvesting energy, transparent OSCs integrated into the rooftop of a greenhouse increased plant fruit production by 20.2% due to beneficial shading effects from UV radiation [7].

1.2 Photonic Power Converters

Photonic power converters (PPCs) are photovoltaic devices similar to solar cells, but are used to convert light to electricity generated from sources other than the sun. Most prominently, PPCs are used within optical fiber networks in order to convert the optical power transmitted through the fiber into electrical power at the destination. Although power transmission through optical fibers is more complex and expensive than conventional power transmission using electricity with metallic wires, it offers two major advantages: protection against electrical power surges and electromagnetic interference.

Surges are transient spikes in the current or voltage in an electrical system. A sudden increase of these can cause detrimental effects to sensitive components within a system. Often these damages are purely economic in nature, but can also pose safety concerns such as in medicine, transportation, or the military. In these cases, electrical isolation is necessary to prevent surges from reaching the sensitive components. Optical power transmission offers total electrical isolation by nature, as the optical link is a dielectric material. At either end of the optical fiber are optoelectronic components that convert optical power to electrical power, and vice-versa. Of these, focus will be given to the receiver on the downstream end of the fiber, the PPC, where light is converted into electricity.

PPCs operate similar to solar cells, where an absorbing semiconducting medium is used to capture the incident radiation. Semiconductor layers are doped and arranged in p-n junctions to drive electrons and holes to opposite electrodes, creating the electric potential necessary to drive external circuits. Of the numerous factors involved in the choice of semiconductor, the design wavelength is amongst the most important. Infrared irradiation near 835 nm is often employed in optical systems due to availability of lasers at this wavelength, and relatively low losses in fibers [8]. For this wavelength, GaAs is a suitable semiconducting media, and also offers the benefit of being a well-studied and widely used material. Current research in PPCs includes the development of devices at longer wavelengths, such as 1310 nm, to decrease the power loss during transmission through optical fibers. For power transmission using

wavelengths less than 870 nm, the optical power loss is approximately 3 dB/km, whereas transmission at 1310 nm has a loss of approximately 0.35 dB/km [9]. One suitable semiconductor candidate is the quaternary blend InAlGaAs, which is currently under development for a working PPC device. One of the goals of the work presented in this thesis is to showcase strategies to improve PPC efficiency for the eventual implementation in these InAlGaAs devices. However, since the material system is still under study, GaAs devices will be used in this work, but the overall strategy can be adapted to the InAlGaAs system in future work.

1.3 Contributions

All work presented within this dissertation was done by the author, except for the following:

- **Chapter 3:** All organic solar cells used, and all materials deposited for ellipsometry were done by Trevor Grant of the Lessard Research Group. Trevor also performed the current-voltage measurements at 1,000 W/m^2, and led much of the analysis on the solar cells under reduced light intensities.
- **Chapter 4:** Dr. Marziyeh Zamiri of the SUNLAB Solar Research Group designed the developed the procedure for contact fabrication on the semiconductor wafers for the photonic power converter devices.

1.4 Organization

The work in this thesis is organized within the proceeding chapters as described below:

Chapter 2 provides all necessary background information contained in chapter 3 regarding organic solar cells, and in chapter 4 regarding photonic power converters. It is assumed that the reader has basic knowledge of inorganic semiconductor devices, but not of organic semiconductor devices. As such, the operating principles of organic solar cells are discussed, including a brief overview of electronic properties of organic molecules. The organic materials examined in this work are introduced.

With regards to photonic power converters, since this technology is not widely known Chapter 2 introduces the technology to expand upon a reader's basic knowledge of inorganic photovoltaics. Multijunction devices and light trapping techniques are addressed.

Chapter 2 also describes the modelling software used for subsequent chapters. Solcore, an open-source package in Python, was used for the optoelectronic modelling of the photovoltaic cells [10]. This software was chosen because of its flexibility as an open-source library, and the accuracy of its

modelling tools as shown in literature. Although Solcore provides numerous software tools, within this work it was primarily used to simulate the optical absorption, and voltage-current relations within photovoltaic cells. Due to the close similarities between solar cells and PPCs, the same modelling toolset could be used for analyses on both systems.

Chapter 3 describes the experimental methodology, analysis, and results of the incorporation of two new semiconductor material blends within bulk heterojunction organic solar cells. The newly studied non-fullerene acceptor $(3BS)_2$-SiPc is demonstrated in a blend with donor P3HT, and compared with a conventional fullerene-based P3HT:$PC_{61}BM$ active layer. The same $(3BS)_2$-SiPc acceptor is also demonstrated with the donor PBDB-T for a system with a large HOMO-LUMO energetic offset, and compared with a PBDB-T:$PC_{61}BM$ device. For all four solar cell devices, the current-voltage and external quantum efficiency characteristics were experimentally measured, including measurements at various angles of incidence and irradiation intensities. Optical models using Solcore were created to simulate the experimental conditions within the solar cell devices, and used to gain insight into wavelength dependencies and absorption profiles. The optical parameters of the four active material blends were obtained through ellipsometry, and used for both the simulations and qualitative analyses.

Chapter 4 focuses on the modelling and design of multijunction photonic power converters. The design process of a 5-junction power converter is outlined, then compared with identical devices incorporating a back reflecting surface for light management. Both metallic and distributed Bragg reflectors were simulated, and the efficiencies and device architectures analyzed. A portion of this chapter is also devoted to describing the experimental processes performed for contact fabrication on physical semiconductor wafers for photonic power converters.

Chapter 5 summarizes the results and analysis given in chapter 3 and chapter 4, along with a brief summary of the optoelectronic simulations performed using Solcore.

2 Chapter II: Background

Chapter 2 contains all relevant background information necessary to understand the methodology, results, and analysis done in chapter 3 and chapter 4. Section 2.1 reviews organic solar cells, and begins with an explanation of the electronic properties of organic semiconductors and how they are used within bulk heterojunction solar cells. The project goals and description are introduced, followed by a description of the new material blends assessed, P3HT:$(3BS)_2$-SiPc, and PBDB-T:$(3BS)_2$-SiPc.

Section 2.2 is about photonic power converters, and introduces both single and multijunction device structures. The electrical current-matching design process is introduced, along with the concept of light trapping techniques for larger efficiencies. Metallic and distributed Bragg reflectors are briefly explained.

Section 2.3 describes the software package Solcore. The transfer matrix method and depletion approximation for optoelectronic simulation are described in some detail.

2.1 Organic Solar Cells

2.1.1 Organic Semiconductors

Organic solar cells convert energy from the sun to electricity through the absorption of light in an organic semiconductor. Organic compounds cover a large category of materials, but is generally accepted to consist of chemical compounds with one or more carbon atoms covalently bonded to other atoms, with at least one carbon-hydrogen bond, although exceptions exist. Most organic material is electrically insulative, but an advantage of organic chemistry is that materials can be engineered and synthesized to have desired properties, such electrical conductivity.

There are two types of bonding molecular orbitals in organic chemistry, σ and π bonds, which arise from atomic orbital overlaps within a molecule. Let us consider pentacene, a common small molecular organic semiconductor, as depicted in Figure 1 [11]. Pentacene has a planar geometric structure where each carbon atom is sp^2 hybridized (a hybrid of the s, p_x, and p_y orbitals), and each sp^2 orbital interacts with an adjacent carbon's sp^2 orbital, or a hydrogen's s orbital. These bonds are denoted as σ bonds, and are formed directly between two atoms. Carbon's fourth orbital, the p_z orbital, is directed out of the plane. These p_z orbitals overlap above and below the plane, indirectly between the carbon atoms, to form π bonds in the system. All 22 carbon atoms within pentacene are said to be conjugated in this

system, where the π bond can be considered to be "shared" between each atom. Electrons in the π orbitals are able to move easily within this conjugated network.

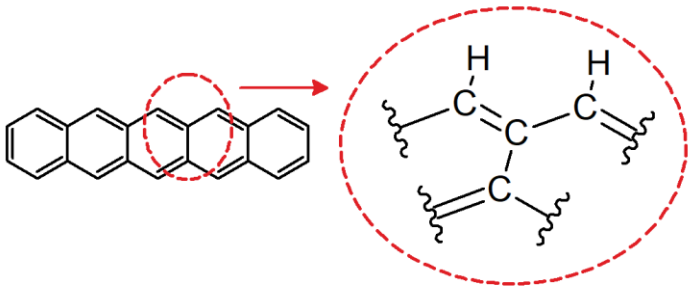

Figure 1: Pentacene molecular structure, displaying the sp^2 hybridization.

Conductive organic materials are π-conjugated compounds that facilitate charge transport intramolecularly through conjugated π orbitals, or intermolecularly through π-π interactions. This intermolecular charge transport occurs when π orbitals from two different molecules overlap, and the charge can "hop" between molecules. It has been shown that hopping distance, and the orientation of the molecules both effect the transport mechanism, where shorter distances and larger overlap increase this transfer [12].

The insulative property of organic semiconductors arises from the energy difference between the compound's highest occupied and lowest unoccupied molecular orbitals (HOMO and LUMO). As such, an organic compound that is electrically conductive through π conjugation, and has a small enough HOMO-LUMO energy gap to allow for charge injection without material degradation, can be considered an organic semiconductor. Typical energy gaps for organic semiconductors are <3 eV, but for solar applications, they are usually chosen to be lower in energy to increase the absorption of the solar spectrum [13]. For example, a semiconductor with a low energy gap of 1.37 eV was used to fabricate a solar cell that absorbed light for wavelengths below 907 nm [14].

2.1.2 Organic Solar Cell Operating Principles

The most common architecture for organic solar cells are based on bulk heterojunction (BHJ) structures [15]. These devices contain a blend of at least two different organic semiconductors to operate, one donor and one acceptor molecule, each with different energy levels. These are placed between two electrodes with a typical thickness of 100 nm, and referred to as the active layer, as depicted in Figure 2 [16,17]. The active layer will absorb sunlight, then charges will be transported to opposite electrodes to allow for operation.

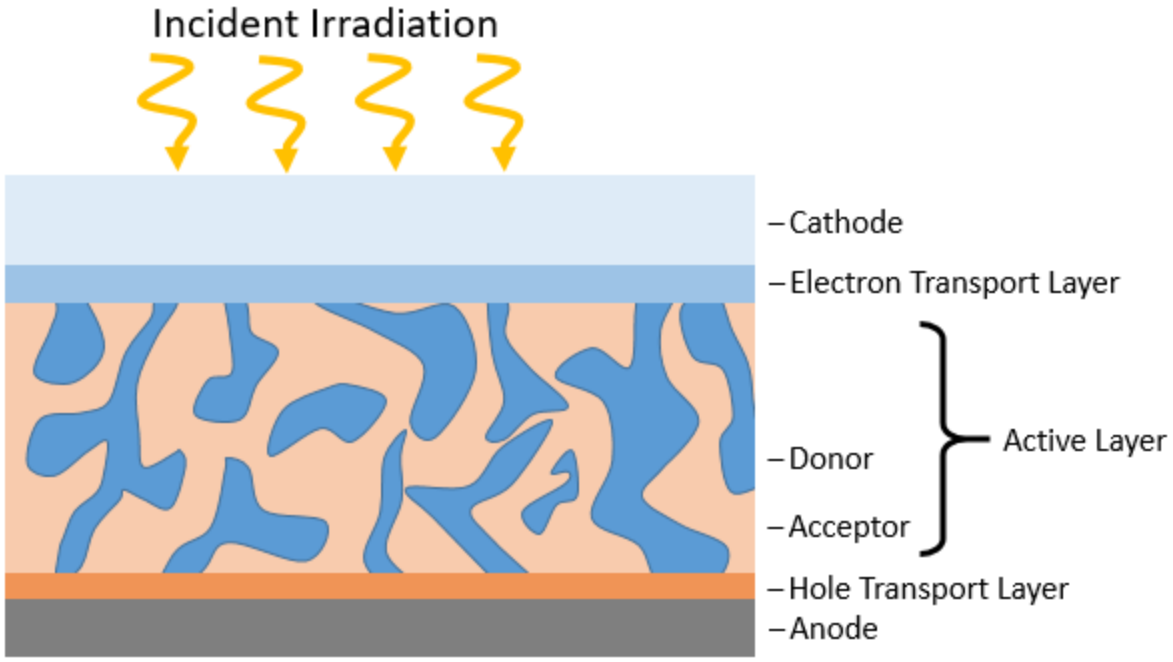

Figure 2: Basic BHJ OSC architecture [17].

The overall operating process of an organic solar cell is shown in Figure 3. During operation, sunlight is shone into the active layer through a transparent electrode, and absorbed by the donor, acceptor, or both. In the case of donor absorption, the donor will absorb light and an electron will excite from the HOMO to the LUMO, as seen in Figure 3a. This "excited" complex is referred to as an exciton, which is the pair between the excited electron and corresponding hole. The exciton will then diffuse to the donor-acceptor interface through energy transfer pathways, which is typically non-radiative for solar cell applications, and depicted in Figure 3b. Charge separation will occur at this interface, where the donor will "donate" its electron to the acceptor molecule, shown in Figure 3c. The LUMO of the acceptor is designed to be lower than that of the donor, and this difference creates a driving force for the electron to "hop" from the donor LUMO to the acceptor LUMO. Generally, the difference is at least 0.2-0.3 eV for effective transfer [18]. For light absorption by an acceptor molecule, the process is identical, except the acceptor provides a hole to the donor molecule, so the donor's HOMO must be greater than that of the acceptor's. Following charge separation, the electron and hole move to opposite electrodes, as in Figure 3d, which creates a potential difference across the electrodes, allowing the solar cell to act as a voltage source when connected to an external load. The conduction bands of the electrodes are aligned with the LUMO of the acceptor and the HOMO of the donor, to maintain the electric potential across the device and facilitate charge transfer. This charge movement illustrated in Figure 3d is facilitated in

part by the difference in work functions of these electrodes, such that the electrons are driven to the electrode with a lower work function [19]. In typical architectures, the transparent electrode (usually indium tin oxide (ITO)) has the larger work function, and acts as the anode (hole collecting layer). These devices typically showcase larger efficiencies, but have stability issues due to the low work function of the cathode [20,21]. Due to this, inverted structures are becoming increasingly common, where the ITO acts as the cathode, and a high work function metal, such as silver, is used as the anode.

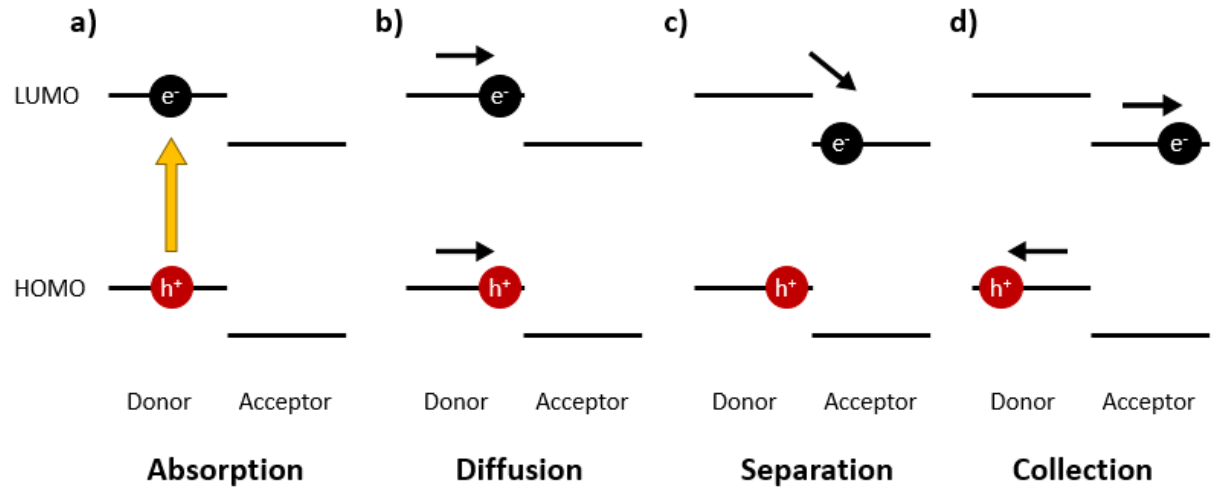

Figure 3: Operation of an organic solar cell, displaying light absorption (a), exciton diffusion (b), charge separation (c), and charge collection (d).

To facilitate charge transfer and inhibit charge recombination within the active layer, which causes charges to bypass the external circuit, electron and hole transport and blocking layers are used [22]. For the electron transport layer, the material is chosen to have a similar LUMO as the acceptor to allow for electron injection to the conduction band of the cathode. For an electron blocking layer, the material is chosen to have a significantly larger LUMO than both the LUMO of the donor and the conduction band of the anode to block electron injection. Similar materials are used for hole transport and blocking layers (opposite of the electron ones), and often the transport layers take on dual roles for electron transport while hole blocking, or vice-versa. In use, these layers promote charge extraction and suppress undesirable recombination, thus enhancing the efficiency of the photovoltaic device.

2.1.3 Bulk Heterojunction Solar Cells

The use of a BHJ layer in OSCs is for ease of manufacture in roll-to-roll solution printing. The donor and acceptor are mixed together, injected onto the cell, thinned to a desired level, then dried to form the completed layer. Each of these steps can be designed to optimize the performance of the cells, but at

the end of the day, this processing technique is designed to be low cost and will not result in a perfect device. To compliment this simple manufacturing technique, inexpensive donor and acceptor material combinations should be researched. Although high performing and inexpensive active layers would be ideal, progress would still be made through active layers that offer cost-reductions and achieve similar or better performances than current active layers on the market.

Although there are many promising donor material candidates for OSCs, poly(3-hexylthiophene) (P3HT) is currently the only donor polymer available on a large scale [23], and is the preferred choice for OSC commercialization if a suitable acceptor is found due to synthetic simplicity [24]. Historically, fullerene derivatives, such as [6,6]-phenyl-C61-butyric acid methyl ester ($PC_{61}BM$), have been used as acceptor materials, but have some drawbacks including low optical absorptivity, manufacturing difficulties, and demanding synthesis and purification [24,25]. The same researchers to state this have defined a figure of merit to determine the commercial viability of P3HT-based OSCs in comparison to a P3HT:PCBM system which involve three factors: the efficiency, stability, and synthetic complexity. In my thesis project, I have helped study a synthetically simple silicon phthalocyanine (bis(tri-*n*-butyl silyl oxide) silicon phthalocyanine ($(3BS)_2$-SiPc)) derivative as a potential inexpensive acceptor in a P3HT-based bulk heterojunction organic solar cell [26].

2.1.4 Silicon Phthalocyanines

Silicon phthalocyanines (SiPcs) are a family of molecules that are strongly absorptive in the 650-700 nm range [27], and have been commercially produced on a large scale for the dye industry [28]. SiPcs have been previously shown to act as a ternary additive in OSCs for charge transfer facilitation [29], and in BHJ OSCs as an acceptor molecule [27,30], but the latter were preliminary studies only and did not sufficiently compare the P3HT:SiPc system with that of the standard P3HT:PCBM system. Additionally, SiPcs have been proposed to be a direct replacement for PCBM due to their HOMO and LUMO levels, as shown in Figure 4 [27]. This is because their LUMOs are slightly higher than that of PCBM, which should allow for a larger V_{OC}, and lower energy losses due to charge separation.

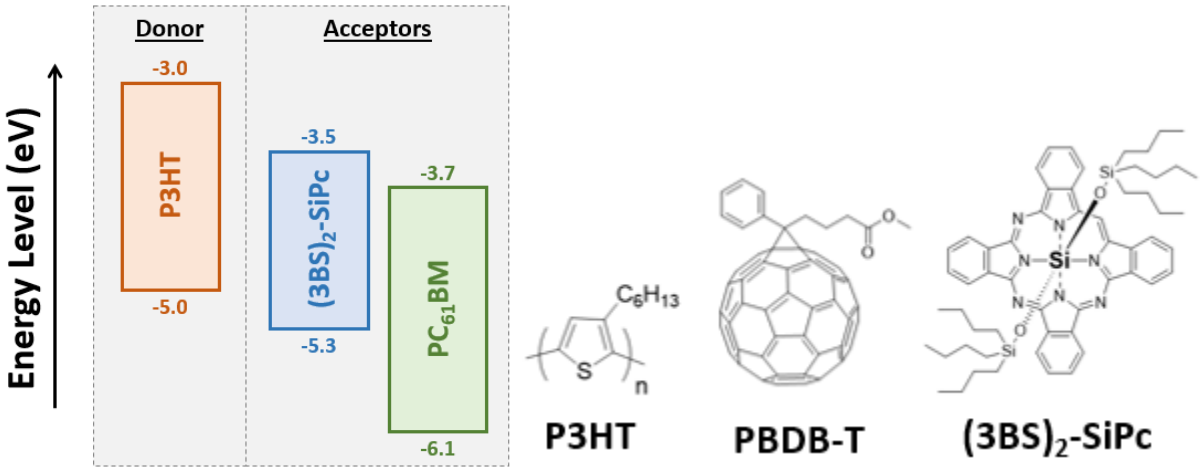

Figure 4: P3HT, $(3BS)_2$-SiPc and PCBM energy levels (left), and their respective chemical structures (right).

First, we will look at the design behind the $(3BS)_2$-SiPc compound, shown in Figure 4, to understand its use as an acceptor molecule. Following this, we will address their synthesis to appreciate why SiPcs are relatively inexpensive acceptor materials.

SiPcs are metal complexes, which involve organic compounds (ligands) that have been coordinated to a metal center. Here, the phthalocyanine ligand is the point of interest. Phthalocyanine is a strongly absorptive chromophore, and with a highly conjugated π-orbital network, offers the optical and electrical foundational framework required for an organic semiconductor. Phthalocyanine is a cycliclar molecule with four nitrogen atoms in the center with sp^2 hybridization, each with one sp^2 orbital directed towards the center of the ring. This makes it a perfect candidate as a chelating ligand (strongly coordinated ligand) for metal complexes. The choice of metal center for this ligand will affect its electronic structure, and its optical and electrical properties. A handful of different combinations of metal centers with phthalocyanine have been studied in literature [31]. Silicon has been noted to be a great candidate because of its high abundance, low toxicity, and low bandgap (ie. relatively stable) [30]. Additionally, the use of silicon allows for two additional ligands to be coordinated to the metal center, which can be chosen to impart desirable chemical and physical properties onto the molecule without changing the complex's overall energetics [29]. To maintain the goals of the project, these axial ligands need retain or increase electrical properties of the material, and allow for solution processability. In previous work, the ligand tri-*n*-butylsilyl oxide was identified to allow high solubility for good processability, while retaining adequate electrical properties due to a strong driving force towards crystallization [27]. Additionally, the strong Si-O bond is a good choice for material stability. The resulting molecule, $(3BS)_2$-SiPc, can be seen in Figure 5 with the silicon metal center, phthalocyanine

chromophore, and tri-*n*-butylsilyl oxide axial ligands. With the tri-*n*-butylsilyl oxide ligands, upon crystallization the $(3BS)_2$-SiPc chromophore arranges with good π-π stacking, which assists with intermolecular charge transport, hence producing good electrical conductivity properties [27].

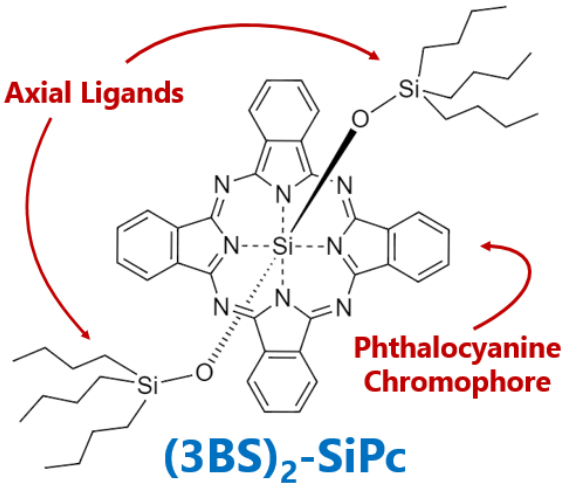

Figure 5: Structure of the SiPc derivative $(3BS)_2$-SiPc, displaying both the phthalocyanine chromophore and the axial ligands. The chromophore is responsible for the optical properties and provides the conjugated π network for electrical conduction, while the axial ligands are responsible for material solubility and assist in forming the crystal structure with π-π overlap.

Since chemical compounds typically have several routes of synthesis, only one route will be mentioned here. Phthalocyanines have been synthesized since the early 1900s, from common reagents such as phthalic anhydride, urea, and metal salts [32]. One such method involves a one-step synthesis 1,3-diimoisoindoline and silicon tetrachloride in quinolone for the production of dichloro silicon phthalocyanine (Cl_2-SiPc), which can be used as a starting material for SiPc derivatives [33]. 1,3-diimoisoindoline is a common chemical that is produced on the industrial scale, but can be synthesized from the ammoxidation of *o*-Xylene (cracking petroleum), followed by the nucleophilic addition of ammonia. Silicon tetrachloride production follows a simpler process through the reaction of chlorine gas with silicon. For the production of $(3BS)_2$-SiPc, Cl_2-SiPc is reacted with tributylchlorosilane (axial ligands), NaOH, and Aliquat HTA-1 in another one-pot synthesis [34]. For illustration, the synthesis starting from phthalonitrile is shown in Figure 6. Overall, the synthesis of metal phthalocyanines is rather simple, and has been estimated to require approximately 2 orders of magnitude less energy than other fullerene-based active materials [27,35].

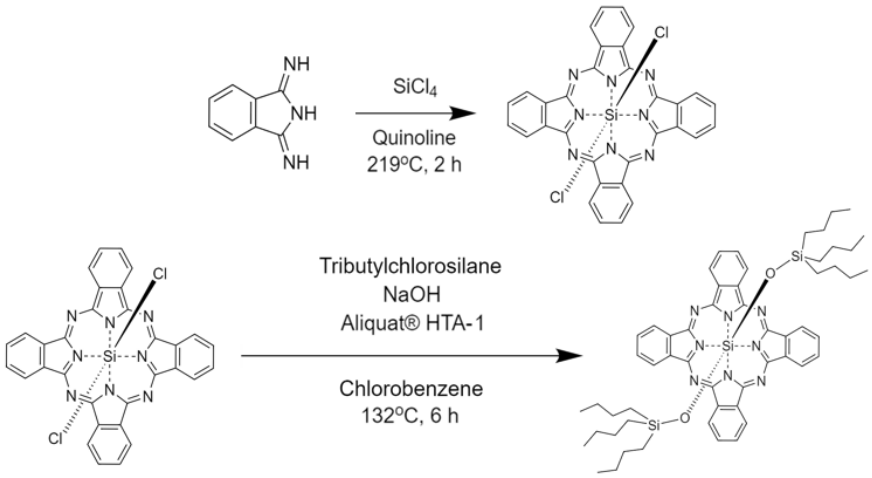

Figure 6: Two-step synthesis of $(3BS)_2$-SiPc, starting from 1,3-diimoisoindoline.

2.1.5 Energy Levels and PBDB-T

Since the voltage of an OSC arises from the difference in energy between the LUMO of the acceptor and the HOMO of the donor, a large energy difference beneficial. Thus, to achieve a high V_{OC}, a donor with a low energy HOMO must be used. The compound poly[(2,6-(4,8-bis(5-(2-ethylhexyl)thiophen-2-yl)-benzo [1,2-b:4,5-b']dithiophene))-alt-(5,5-(1',3'-di-2-thienyl-5',7'-bis(2-ethylhexyl)benzo[1',2'-c:4',5'-c']dithiophene-4,8-dione)] (PBDB-T), is known to be a high performing donor polymer with a HOMO energy level of approximately -5.28 eV, with a LUMO of -3.48 eV [36]. These energy levels nearly match that of $(3BS)_2$-SiPc, so a device was proposed of a PBDB-T:$(3BS)_2$-SiPc to create a high voltage, low loss organic solar cell. The energy levels for PBDB-T and the acceptors can be seen in Figure 7, along with the molecular structure of PBDB-T.

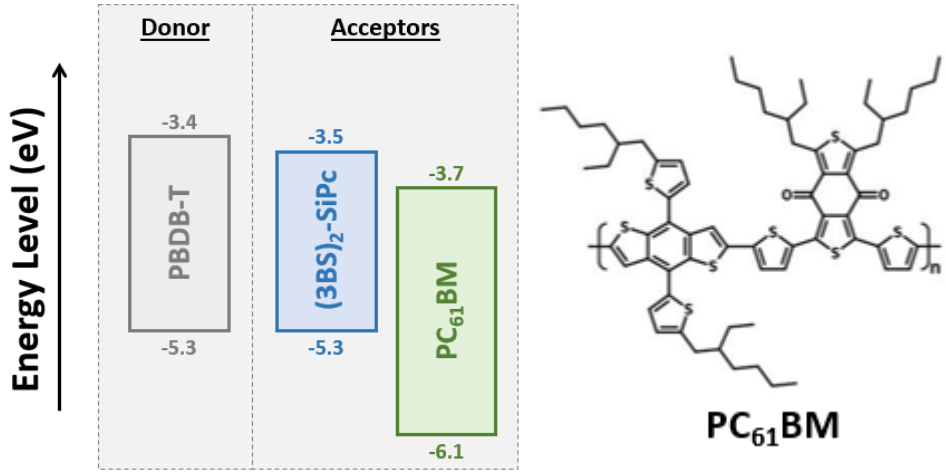

Figure 7: PBDB-T, $(3BS)_2$-SiPc and PCBM energy levels (left), and PBDB-T's respective chemical structure (right).

2.2 Photonic Power Converters

2.2.1 Single Junction PPC Design

Photonic power converters function very similarly to solar cells with one main benefit, the design wavelength. PPCs are designed to operate over a narrow bandwidth at a particular wavelength, rather than the wide spectrum used by conventional solar cells. This allows for an easier optimization of the optical thickness of the PPC junctions, in addition to the antireflection coating selection used at the top of the device.

A typical p-n junction design for PPCs consists of four layers: a front surface field, emitter, base, and back surface field. The emitter and base form the p-n junction required for operation, while the surface fields act to reduce surface recombination, which increases the total amount of available charges for collection at the electrodes [37]. In this work, the emitter is considered to be n-doped, while the base is p-doped. For this configuration, the front and back surface fields have doping levels of n+ and p+, respectively. The general structure of a single junction device can be seen in Figure 8.

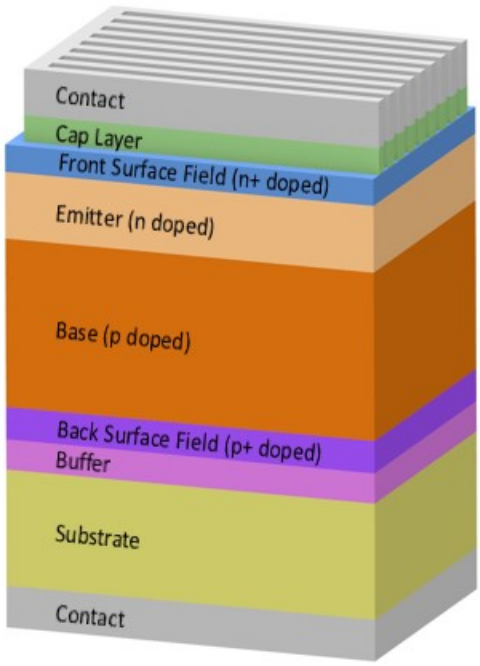

Figure 8: General structure of a single junction photonic power converter (not to scale). The junction is comprised of the front surface field, emitter, base, and back surface field.

The emitter and base consist of the absorbing semiconducting material, with a bandgap corresponding to the design wavelength. As stated previously, for absorption at 835 nm (the wavelength of interest), a

GaAs material can be used. The design thickness of active layers can be determined through optimization of the absorbed power and the recombination losses, as these both increase with thickness. The relative thicknesses of the emitter and base layers can then be optimized such that the interface exists within the diffusion length of a large amount of generated carriers. For new material systems without thoroughly studied recombination properties, the aforementioned optimization cannot be used for the initial design process. For this, the Beer-Lambert law can be used to design the total p-n junction thickness based off a predetermined percentage of light absorption, 99% here, and the relative thicknesses of the emitter and base estimated from this law.

The purpose of the front and back surface fields is for efficiency improvement, and are not intended for current generation. As such, the materials used for these are required to have transparency at the design wavelength. A material system lattice matched to the absorbing semiconductor with a larger bandgap is used for this purpose. Often, one or more of the elements used in the absorbing semiconductor is blended with other elements to achieve this purpose.

2.2.2 Multijunction PPC Design

Multijunction PPCs expand upon the single junction design, where p-n junction are stacked vertically upon one another. The main reasons to incorporate this design are for voltage and efficiency. As per Kirchhoff's voltage law, connecting the p-n junctions in a series configuration allows the total voltage to equal the summation of voltages for all individual p-n junctions. This is beneficial for the end device, as the output voltage can be tailored to the target application. For example, 20 junction GaAs devices have been reported to have an operating voltage approaching 24 V [38].

The incorporation of multiple vertically-stacked junctions within a device subsequently allows for an improvement in efficiency. The total thickness of the PPC is fixed by the total absorbance of light in the device, so the thickness of every junction in the PPC must add up to this total amount. This means that for every additional junction in the device, the thicknesses of the respective junctions must decrease. Consequentially, this decrease in thickness allows for an increase in efficiency due to lower recombination losses.

Due to Kirchhoff's current law, the thicknesses of each junction must be designed to be current matched within the device. Since the junctions are electrically connected in series, the electrical current through each must be equal. Thus, the PPC's maximum power will be limited by the junction with the lowest current [39]. To suppress this limitation, PPCs are designed to output the same electrical current in each

and every junction. For semiconductors with well-known properties, this can be done through an optimization of the junction's thickness using the carrier generation and recombination rates. Conversely, for a new material system, the thicknesses can be estimated by matching the optical absorbance within each junction. Using the Beer-Lambert Law and defining a total absorbance, A_T, the thickness w_i of each of n junctions can be estimated from each junction's absorbance, A_i. For this estimate, the absorption coefficient, α, at the design wavelength, λ, is used.

Due to equivalent absorbance, each absorbance A_i is equal within every layer i, where the summation equals the total absorbance A_T, as shown in Equations (2.1) and (2.2).

$$A_1 = A_2 = \cdots = A_n \quad \text{Equation (2.1)}$$

$$\sum_{i=1}^{i=n} A_i = nA_i = A_T \quad \text{Equation (2.2)}$$

The Beer-Lambert law can then be written relating the intensity I at a given position w to the incident intensity I_0, as in Equation (2.3) [40]. The ratio I/I_0 is representative of the transmittance in a homogenous medium, and under the assumption of negligible reflection between layers, the transmittance can be substituted by 1-A, as in Equation (2.4). The absorption coefficient, α, can also be related to the imaginary part of the complex index of refraction at the design wavelength, $k(\lambda)$, shown in Equation (2.5). In this model, the semiconductor layers are designed to be the same composition as each other with the same absorption coefficient.

$$\frac{I}{I_0} = e^{-\alpha w} \quad \text{Equation (2.3)}$$

$$1 - A = e^{-\alpha w} \quad \text{Equation (2.4)}$$

$$\alpha = \frac{1}{2\pi k(\lambda)} \quad \text{Equation (2.5)}$$

If the absorbance is now written as the cumulative absorbance up to, and including, junction i, the Beer-Lambert law can be modified to Equation (2.6). A simple rearrangement can solve for w_i, the thickness of junction i upon an absorbance matched PPC design, and shown in Equation (2.7).

$$1 - \sum_{j=1}^{j=i} A_j = e^{-\alpha(\lambda)\sum_{j=1}^{j=i} w_j} \quad \text{Equation (2.6)}$$

$$w_i = -\frac{\ln\left(1-\sum_{j=1}^{j=i} A_j\right)}{\alpha(\lambda)} - \sum_{j=1}^{j=i-1} w_j \quad \text{Equation (2.7)}$$

Due to the logarithmic relation of thickness to cumulative absorbance, the thickness of each subsequent junction beyond the first has a larger thickness. This is displayed in Figure 9 for 1-, 2-, and 5-junction devices.

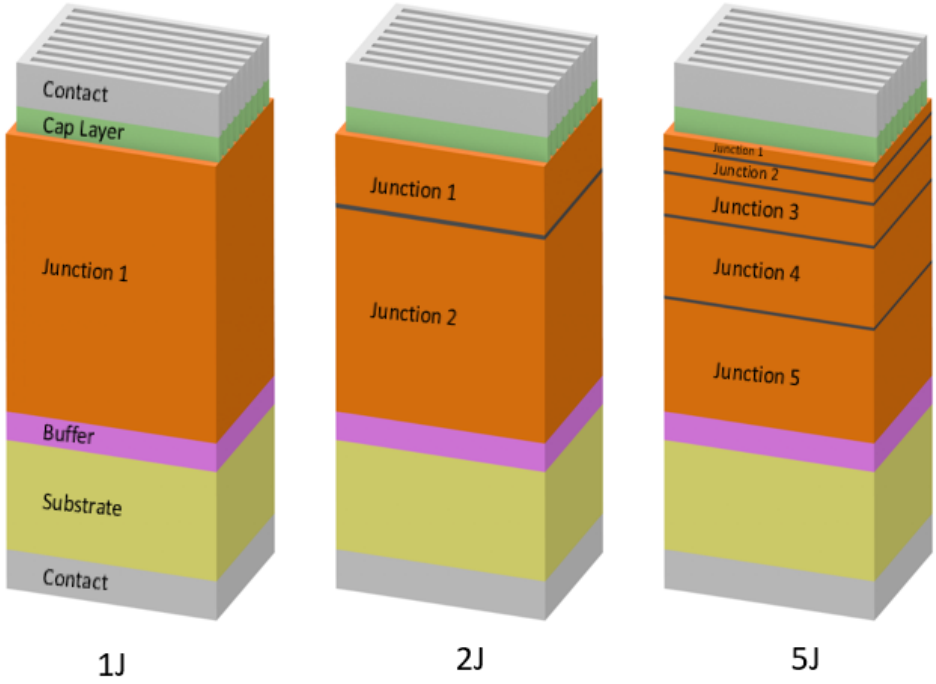

Figure 9: Multijunction photonic power converters, with 1, 2, and 5 junctions, where each junction is separated by a tunnel diode. It can be seen that the total thickness of the structure remains the same regardless of the number of junctions, and that junction thickness increases with depth within the device.

2.2.3 Light Trapping

As mentioned previously, thicker junctions have lower efficiencies due to enhanced recombination effects. A strategy to mitigate this effect is to introduce light trapping techniques within the PPC to decrease the thickness, while retaining the same total absorption [41]. One technique is to place a reflecting or scattering surface at the rear of the device. It has been reported in literature that the use of a perfect reflector at the rear of the device improves a PPC's efficiency, in addition to reducing the amount of material used [41]. Two common reflecting surfaces for photovoltaics are distributed Bragg reflectors (DBR) and metallic reflectors, as shown in Figure 10. The implementation of these reflectors in a PPC will be demonstrated in this work.

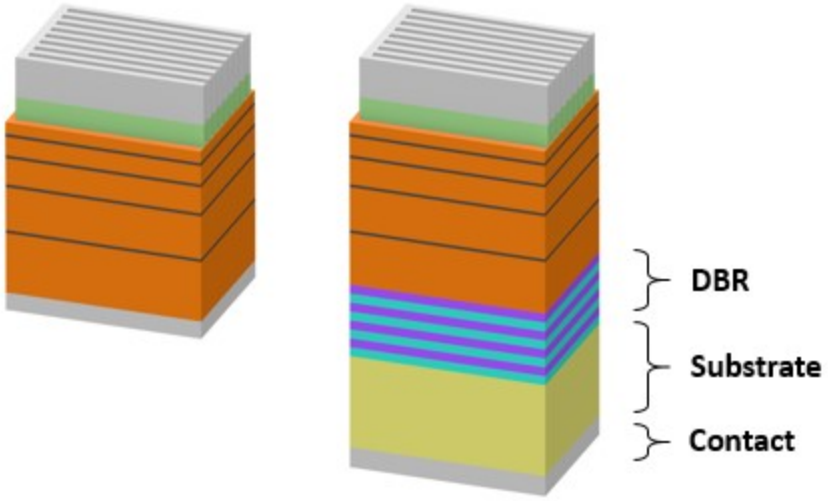

Figure 10: Photonic power converters with a metallic reflector (left), and a distributed Bragg reflector (right), at the rear of the device.

Placement of the reflecting surfaces is important for proper implementation, and is dependent upon the PPC architecture. The surface can be placed anywhere underneath the last p-n junction. However, since photovoltaics are grown on a substrate, placing the target surface underneath the substrate may induce large losses, and counter any benefit to the light trapping technique. If the substrate is absorbent at the design wavelength, techniques may be employed to incorporate the surface immediately following the last p-n junction. The architectures in Figure 10 demonstrate the addition of the reflective surface below the last junction.

Metallic reflectors are perhaps the simplest reflector, where a blanket sheet of metal is deposited on the surface, and acts as both a reflector and an electrode. Since an electrode is required for operation, this technique can be readily employed on PPCs. If an absorbing substrate is required for semiconductor growth, then epitaxial lift-off techniques can be used to separate the substrate from the p-n junctions following growth. This involves the incorporation of a sacrificial layer between the substrate and bottom back-surface field during growth, and a subsequent etch of the sacrificial layer post-growth, as shown in Figure 11. For fabrication, this allows for the direct deposition of the metallic contact underneath the PPC's final junction.

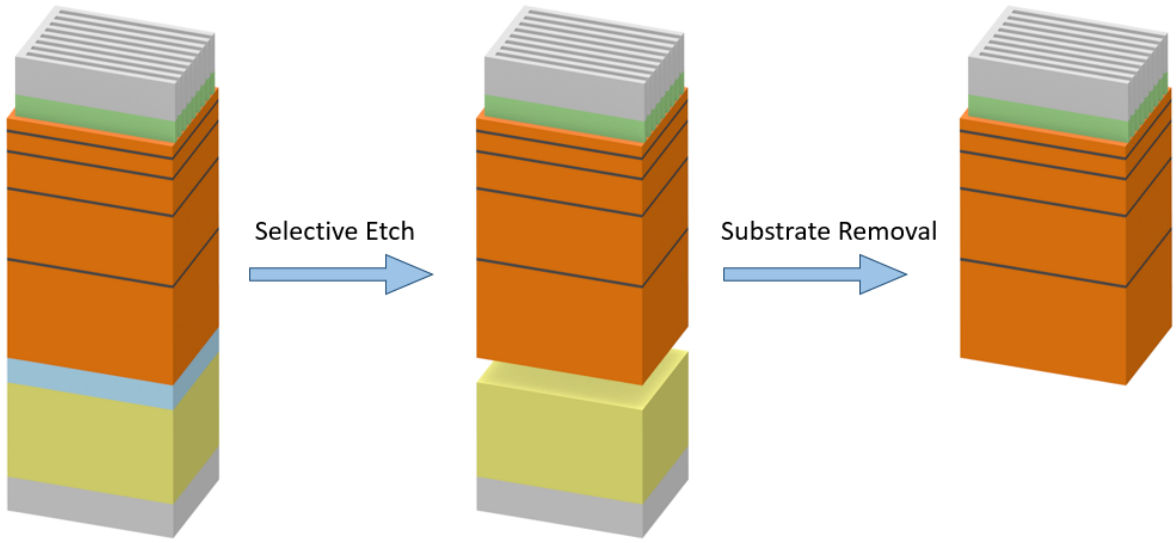

Figure 11: The epitaxially lift-off technique, where a sacrificial layer is introduced between the substrate and the active device during semicontuctor growth. This layer can be removed using a selective etch prior to contact fabrication, which allows for the direct fabrication of a reflective surface beneath the device.

Another type of reflecting surface that can be used is the DBR. This incorporates alternating dielectric layers with different refractive indices to create a photonic bandgap with high reflective properties, as shown in Figure 10. The thicknesses of the alternating layers, in addition to the number of layers used, can be optimized to allow for high reflectivity at the PPC design wavelength. The DBR can be incorporated during semiconductor growth, and post-growth fabrication steps can be performed as usual.

2.3 Optoelectronic Simulations with Solcore

2.3.1 Defining the Physical System

Photovoltaic cells were created in Solcore as a stack of planar layers of uniform materials. For this, a *Structure* object was created to represent the photovoltaic cell, and to contain all the information regarding each individual layer.

Initially, uniform *Material* objects were created, and contained all the relevant optoelectronic and physical properties of the represented material. The properties of the materials used were taken from Solcore's material parameters database, unless otherwise specified [42–45]. *Layer* objects were then created, which contained the *Material* information, geometric (depth) information, and information regarding the role of the layer within the *Structure* object. The *p-n* junctions of the photovoltaic cells

were constructed as *Junction* objects, which grouped the relevant *Layer* objects together along with pertinent parameters relating to the optoelectronic simulations. Both *Layers* and *Junctions* were combined into a *Structure* to represent the photovoltaic cell. Solcore's optical and electrical simulators perform operations using the described *Structure* to determine the photovoltaic cell's performance. The aforementioned process of defining a *Structure* object in Solcore is displayed in Figure 12.

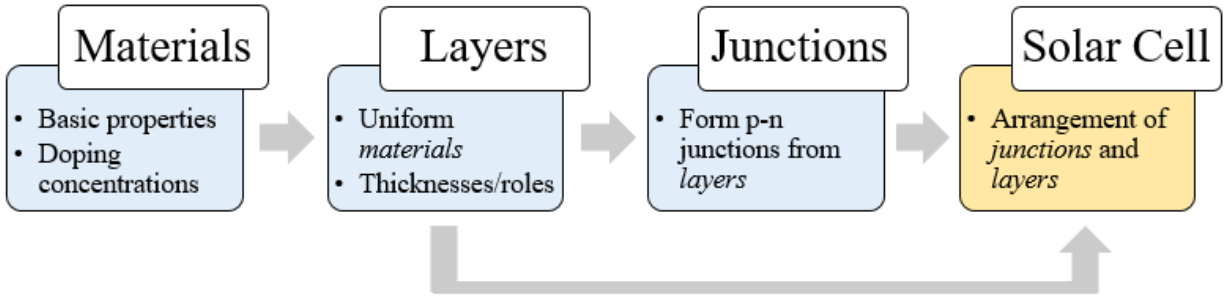

Figure 12: Process to define a solar cell object in Solcore.

2.3.2 Absorbance Modelling

Absorbance modelling in Solcore was done by the transfer matrix method (TMM). The TMM calculates the reflectance, absorbance, and transmission (RAT) in a system of planar layers of specified materials with defined *n* and *k* optical parameters at a given angle of incidence. The Solcore library uses the "tmm" Python package, written by Dr. Steven Byrnes, as the basis for calculations [46]. The relevant equations and derivations can be found in his publication, but below contains a brief summary of the method [46].

The TMM is a way to calculate the optical properties of multilayer planar stacks of materials. This method reduces the effects of the stack to a 2x2 matrix *M*, which relates the reflectance *r* to the transmittance *t*, as shown in Equation (2.8).

$$\begin{pmatrix} 1 \\ r \end{pmatrix} = M \begin{pmatrix} t \\ 0 \end{pmatrix} \qquad \text{Equation (2.8)}$$

The matrix *M* can be related to the depth and optical properties of each layer. For each *n* in *N* layers, the transmittance v_n (forward propagating wave) and reflectance w_n (backwards propagating wave) can be represented by Equation (2.9), where matrix M_n can be found by Equation (2.10). The propagation of these waves is given by the wave equation. The variable δ describes the electromagnetic wave propagation through the n^{th} layer, which can be described through Equation (2.11), where z_n is the layer

thickness, λ_{vac} is the vacuum wavelength, θ is the angle of incidence, and $\tilde{n}$ is the complex refractive index.

$$\begin{pmatrix} v_n \\ w_n \end{pmatrix} = M_n \begin{pmatrix} v_{n+1} \\ w_{n+1} \end{pmatrix} \quad \text{Equation (2.9)}$$

$$M_n = \begin{pmatrix} e^{-i\delta_n} & 0 \\ 0 & e^{i\delta_n} \end{pmatrix} \begin{pmatrix} 1 & r_{n,n+1} \\ r_{n,n+1} & 1 \end{pmatrix} \frac{1}{t_{n,n+1}} \quad \text{Equation (2.10)}$$

$$\delta_n = z_n \, k_z = z_n \frac{2\pi\tilde{n}}{\lambda_{vac}} (\cos\theta \, \hat{z} + \sin\theta \, \hat{x}) \quad \text{Equation (2.11)}$$

To determine *M*, the M_n values for each of the thin films can combined through matrix multiplication, excluding the last layer. This can be seen in Equation (2.12), where the matrix for layer 0 (the incident medium) is shown explicitly.

$$M = \frac{1}{t_{0,1}} \begin{pmatrix} 1 & r_{0,1} \\ r_{0,1} & 1 \end{pmatrix} \prod_{i=1}^{N-2} M_i \quad \text{Equation (2.12)}$$

To get the transmittance and reflectance of light from the optical stack, Equation (2.10) and Equation (2.12) can be substituted into Equation (2.8). After this, the absorption *a* can be calculated from the relation $a = 1 - r - t$ to fully describe the system. The inputs to this system are the number of layers *N*, the thicknesses of each layer z_n, and the complex refractive index for each layer $\tilde{n}$.

2.3.3 Electrical Modelling

Following the optical simulation, the electrical properties of the photovoltaic system were attained using the depletion approximation. This method uses a semi-analytical solution to the Poisson-drift-diffusion equations, which can use macroscopic inputs such as charge mobilities, diffusion lengths, recombination rates, and dopant concentrations.

Photovoltaic devices are comprised of *p*-*n* junctions, which provide the foundation for operation. When a *p*-type material (electron deficient) is brought into contact with an *n*-type material (electron surplus), electrons diffuse from the *n*-type material into the *p*-type material due to the concentration gradient. Similarly, holes diffuse from the *p*-type material to the *n*-type material. This movement creates a charge imbalance between the two materials, where the *p*-type material becomes negatively charged due to the influx of electrons (and the *n*-type becomes positively charged), which causes the formation of an electric field at the junction. This region containing excess charges is called the depletion region. The depletion zone is of finite length, because at steady-state conditions, the diffusion of charge in one direction is balanced by the electric field forcing charge movement in the opposite direction.

In the depletion approximation, it is assumed that there are no free carriers within the depletion zone, and that the intrinsic electric field is due to the ionized *n* and *p* dopants [10]. Outside of the depletion zone, yet still within the *p*-*n* junction, the material is assumed to retain a neutral charge with a constant electric potential. As a result of this approximation, an analytic solution for the photovoltaic cell can be derived from Poisson's equation along one dimension, which relate the electrostatic potential to the electrical charges within the system. The solution is separated into four parts: the neutral region within the *p*-type material, the depletion zone within the *p*-type material, the depletion zone within the *n*-type material, and the neutral zone within the *n*-type material. Poisson's equation can be used to determine the electric potential within the depletion zone, and then the transport equations can be solved with knowledge of the potential.

To solve Poisson's equation along one dimension, let the *z* axis represent the normal to the *p*-*n* junction with the origin lying at the interface of the two materials, and with the positive axis aligned with the *n*-type material. Poisson's equation can be seen in Equation 2.13, where φ represents the potential, ϵ_s represents the material's permittivity, *q* a unit charge, *p* and *n* the density of ionized acceptors and donors, and N_D and N_A the density of the free electrons and holes [10,47].

$$\frac{d}{dz}\left(\epsilon_s \frac{d\phi}{dz}\right) + q(p - n + N_D - N_A) = 0 \qquad \text{Equation (2.13)}$$

Under the depletion approximation, *p* and *n* are assumed to equal 0 and the assumption of a constant permittivity, Equation 2.13 can be rearranged to Equation 2.14. The variable ρ represents the charge density of the carriers within the junction.

$$\frac{d}{dz}\left(\epsilon_s \frac{d\phi}{dz}\right) = q(N_A - N_D) = \rho(z) \qquad \text{Equation (2.14)}$$

The width of the depletion zone within the *p*-type material can be represented by w_p, and the width in the *n*-type material represented by w_n. The charge density within each of the aforementioned four regions of the depletion zone can be represented by constant values, and are shown in Equation 2.16.

$$\rho(z) = \begin{cases} 0 & \text{for} \quad z < -w_p \\ -qN_A & \text{for} \quad -w_p < z < 0 \\ qN_D & \text{for} \quad 0 < z < w_n \\ 0 & \text{for} \quad w_n < z \end{cases} \qquad \text{Equation (2.16)}$$

After substitution of Equation 2.16 into 2.15 and completion of the integrals, the electric potential can be determined using Equation 2.17. It is assumed that the potential of the *p*-doped material is 0 V, and the potential of the *n*-doped material is V_{bi}, the built-in voltage across the device.

$$\phi(z) = \begin{cases} 0 & \text{for} \quad z < -w_p \\ \frac{qN_a}{2\epsilon_s}(z + w_p)^2 & \text{for} \quad -w_p < z < 0 \\ V_{bi} - \frac{qN_d}{2\epsilon_s}(z - w_n)^2 & \text{for} \quad 0 < z < w_n \\ V_{bi} & \text{for} \quad w_n < z \end{cases} \qquad \text{Equation (2.17)}$$

The built-in voltage, shown in Equation 2.18, is assumed to be constant within the device, and related to the doping concentrations N_A and N_D, the temperature T, and the intrinsic carrier concentration n_i, where k_b is the Boltzmann constant. The widths w_p and w_n can be determined using Equation 2.17 and using the knowledge that the electric potential must be continuous at z=0.

$$V_{bi} = \frac{k_b T}{q} \ln\left(\frac{N_D N_A}{n_i^2}\right) \qquad \text{Equation (2.18)}$$

The transport equations for the current densities J_n and J_p of carriers in the *n*-doped and *p*-doped regions can then be calculated using Equation 2.19 and 2.20, where μ represents the carrier mobility.

$$J_n = q\mu_n\left(-n\frac{d\phi}{dz} + \frac{k_B T}{q}\frac{dn}{dz}\right) \qquad \text{Equation (2.19)}$$

$$J_p = q\mu_p\left(-p\frac{d\phi}{dz} + \frac{k_B T}{q}\frac{dp}{dz}\right) \qquad \text{Equation (2.20)}$$

To fully describe the performance of the photovoltaic device, the continuity equations shown in Equations 2.21 and 2.22 can be used, where G and R are the generation and recombination rates of carriers in the process.

$$\frac{dJ_n}{dz} + qG - qR = 0 \qquad \text{Equation (2.21)}$$

$$-\frac{dJ_p}{dz} + qG - qR = 0 \qquad \text{Equation (2.22)}$$

Using the depletion approximation and associated equations, the open circuit voltage (V_{OC}) and short circuit current (I_{SC}) can be determined. These two parameters are important for photovoltaic analyses, as they relate to the voltage and power output of the device. Of specific note, the short circuit current density (J_{SC}) is an important property to compare between similar devices with the same V_{OC}, as a larger J_{SC} can correlate with a larger power output.

3 Chapter III: Organic Solar Cells

Chapter 3 regards the experimental procedure, results, and analysis of the two new bulk heterojunction active layers for organic solar cells. Section 3.1 describes the experimental procedures used for fabrication, testing, and ellipsometry on the devices, and is followed by section 3.2 providing results and discussion. Details on device performance are discussed under standard conditions, at increasing angles of incidence, and under reduced light intensities. The external quantum efficiency is discussed, and related to the optical parameters of the active layer blends. Absorbance simulations using Solcore were done to model the organic solar cells, and the results related to the experimental results.

3.1 Experimental

3.1.1 Fabrication

The bulk heterojunction solar cells were designed and fabricated as an inverted structure on a soda-lime glass slide. A representation of the device is displayed in Figure 13. Zinc oxide (ZnO) is used as an electron transport layer and hole blocking layer, while molybdenum oxide (MoO_x) as an electron blocking and hole transport layer.

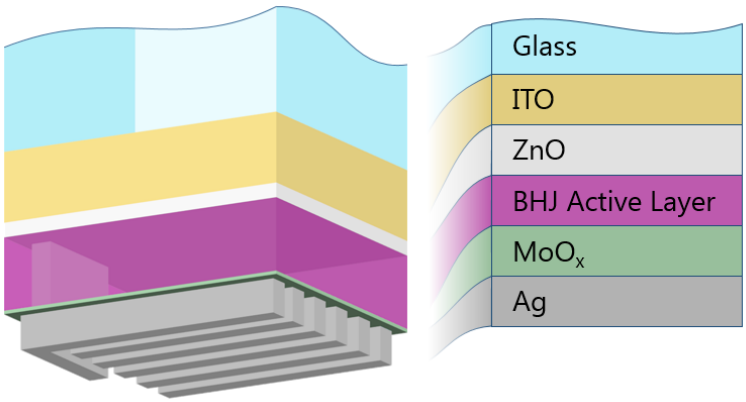

Figure 13: Architecture of the fabricated organic solar cells.

Soda-lime glass slides with a 145 nm thin film of ITO purchased from Thin Film Devices Incorporated were used as the substrate for device fabrication. These were cleaned with sequential baths of soap-water, water, acetone, and methanol in a sonicator for 5 minutes, then dried in air plasma for 15 minutes. The ZnO and active layer solutions were premixed prior to fabrication. The ZnO solution was prepared with 0.1956g zinc acetate dehydrate, 6 mL of ethanol, and 0.054 mL of ethanolamine stirred for 1 h at 50°C. The active layer solutions were mixed in 1,2-dichlorobenzene, and mixed to a

donor:acceptor ratio of 1:1 by weight. The P3HT solutions had a polymer concentration of 20 mg/L and stirred for 4 h at 50°C, while the PBDB-T devices were prepared with a polymer concentration of 10 mg/L and stirred for 4 h at 35°C. Diiodooctane was added to the PBDB-T/$PC_{61}BM$ solutions at a concentration of 3% by volume 1 h before spin coating.

For fabrication, the ZnO layer (30 nm) was spin coated at 2000 rpm for 1 minute onto the plasma treated glass slide and baked at 180°C for 1 h. The device was then moved into a glove box with a nitrogen atmosphere for the following processing steps. The active layers were then spin casted at different processing conditions, and shown in Table 1. MoO_x and silver (Ag) were then deposited by physical vapor deposition. A shadow mask was used during this step to pattern the device, where five separate contacts with an area of 0.325 cm^2 were created for the five devices, and a sixth to contact the ITO layer (as represented in Figure 13). Prior to physical vapor deposition, the active material and ZnO layers were scratched off underneath a portion of this "sixth" contact to allow for direct contact with ITO, which can be seen in Figure 13.

Table 1: Spin coating processing conditions.

	Spin Rate (s)	Spin Time (nm)	Thickness (nm)
P3HT/PCBM	1200	35	150
P3HT/SiPc	1500	90	150
PBDB-T/PCBM	1000	60	80
PBDB-T/SiPc	1000	60	80

Following fabrication, the devices were tested under 1,000 W/m^2 while still in the glove box. The devices were then encapsulated by placing a glass slide on top of the silver layer (inverted structure) with a Norland NOA61 optical adhesive before removal from the glove box for further testing. A conductive silver paste was applied to the exposed metal contacts to allow for electrical contact with the testing apparatuses.

3.1.2 Current-Voltage and External Quantum Efficiency

The electrical characteristics of the OPV devices were determined through current density-voltage (*J-V*) measurements. As alluded to previously, these were taken with two different solar simulators. The first, used during device fabrication in a nitrogen environment, was an Abet Technologies Sunlite 11002 solar simulator for measurements at 1,000 W/m^2. The second, used for encapsulated devices under

ambient conditions, was a Newport Oriel Sol3A-CPV solar simulator with an AM1.5G filter. Variable intensity measurements were performed through the adjustment of a continuously-variable aperture to allow intensities from 100-850 W/m^2, and an OD1.0 filter was used in combination with the aperture for intensities lower than 100 W/m^2. A custom stand was used to allow for adjustments in the tilt angle of the device, where the device was tilted in relation to the collimated light from the solar simulator.

The experimental setup for the Sol3A solar simulator is shown in Figure 14 (left) and Figure 15. The OPV device was mounted on a chuck, and custom DIP clips used to establish electrical contact with the device. Alligator clips are shown here, but were replaced with the DIP clips for a softer clamping action on the delicate silver electrodes. The platform rotates along an axis running left-right from 0-80^o, and a digital level was used to measure the tilt angle. A reference solar cell was used to measure the intensity of radiation at 0^o tilt, and cosine losses were taken into account at each angle of incidence.

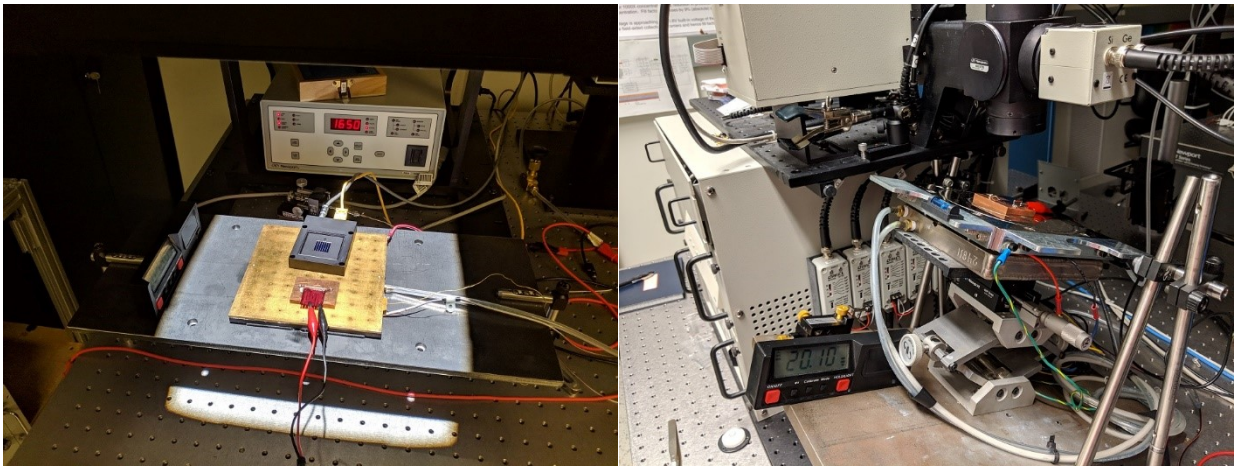

Figure 14: J-V (left) and EQE (right) experimental setups, displaying the custom tiltable stands.

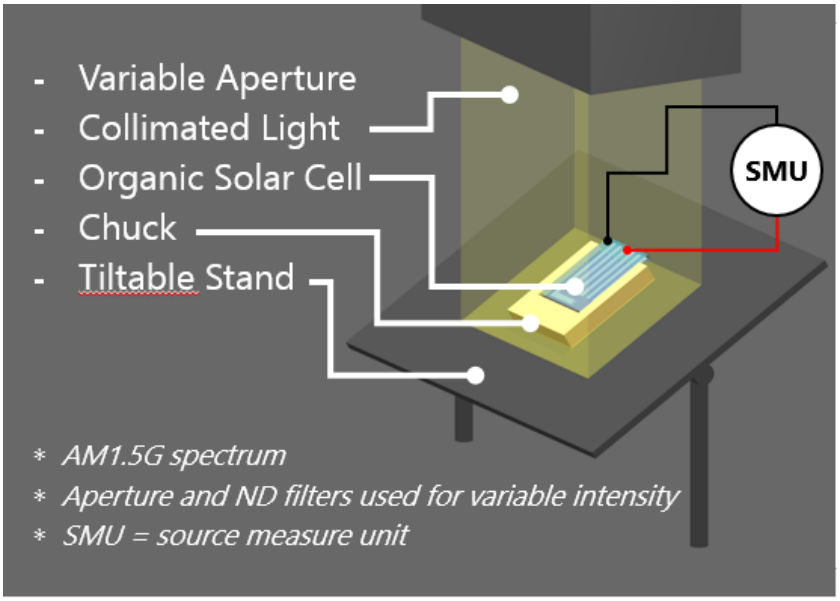

Figure 15: Diagram of the J-V experimental setup.

The external quantum efficiency of the OPV devices were measured using a modified Newport Oriel IQE 200 over the range of 300-800 nm at 10 nm increments. A custom stand was used to allow for adjustable angles of tilt from 0-40°, which were measured with a digital level, as shown in Figure 14 (right). Due to the relatively small spot size of the beam, cosine losses were not accounted for during these measurements.

3.1.3 Ellipsometry

A Horiba UVISEL spectroscopic phase modulated ellipsometer with DeltaPsi2 software was used to measure the refractive index (*n*) and extinction coefficient (*k*) of the OPV materials. These were done over the range 300-900 nm in 10 nm increments at an incidence angle of 70°. The materials used for fabrication of the solar cell were measured, except for molybdenum dioxide and silver. Excluding the ITO/glass slide, all materials were spin coated onto a substrate with identical processing conditions as the device fabrication, where ZnO used an ITO/glass substrate, and all other materials used a characterized soda-lime glass slide. The Cauchy Absorbent model was used to determine the thickness of the films over 800-900 nm, and verified with a Dektak profilometer for all organic layers [48]. This model can be used to fit ellipsometry data of weakly, or non-absorbing media, and provided adequate fits for the measured films over the given range. The Cauchy Absorbent model can be seen in Equation (3.1), where *A, B, C, D, E,* and *F* are constants.

$$\begin{cases} n(\lambda) = A + \frac{10^4 * B}{\lambda^2} + \frac{10^9 * C}{\lambda^4} \\ k(\lambda) = 10^{-5} * D + \frac{10^4 * E}{\lambda^2} + \frac{10^9 * F}{\lambda^4} \end{cases}$$ Equation (3.1)

Following thickness verification, the materials were characterized over the range 300-800 nm using other methods. The New Amorphous Dispersion Formula was used to provide a fit for all materials except for P3HT, PBDB-T, and $(3BS)_2$-SiPc, in which a point-by-point extraction was used. The New Amorphous Dispersion Formula is used to characterize dispersive media containing oscillators, and has been used by the manufacturer for measurements on organic semiconductors and long-chain molecules [49]. This method was also used to roughly characterize P3HT, PBDB-T, and $(3BS)_2$-SiPc prior to the point-by-point extraction for a more accurate fit. The New Amorphous Dispersion Formula can be seen in Equation (3.2) where ω_j is the energy band gap, N is the number of oscillators, and ω_j, Γ_j, and f_j are oscillator specific constants. The constants B_j and C_j are given by Equations (3.3) and (3.4).

$$\begin{cases} n(\omega) = n_\infty + \sum_{j=1}^{N} \frac{B_j(\omega-\omega_j)+C_{1j}}{(\omega-\omega_j)^2+\Gamma_j^2} \\ k(\omega) = \begin{cases} \sum_{j=1}^{N} \frac{f_j(\omega-\omega_g)^2}{(\omega-\omega_j)^2+\Gamma_j^2} & ; \ for\ \omega > \omega_g \\ 0 & ; \ for\ \omega \le \omega_g \end{cases} \end{cases}$$ Equation (3.2)

$$B_j = \frac{f_j}{\Gamma_j}\left(\Gamma_j^2 - \left(\omega_j - \omega_g\right)^2\right)$$ Equation (3.3)

$$C_j = 2 f_j \Gamma_j (\omega_j - \omega_g)$$ Equation (3.4)

All experimental values for n and k were used in the optical simulations for the solar cells except MoO_3 and Ag, which were taken from literature [45,50].

3.2 Results and Discussion

3.2.1 Device Performance

As described previously in the introduction, bis(tri-*n*-butlysilyl oxide) silicon phthalocyanine ($(3BS)_2$-SiPc) is proposed as a direct replacement of the acceptor [6,6]-phenyl-C61-butyric acid methyl ester (PCBM) in bulk-heterojunction organic photovoltaics. Additionally, poly[(2,6-(4,8-bis(5-(2-ethylhexyl)thiophen-2-yl)-benzo[1,2-b:4,5-b']dithiophene))-alt-(5,5-(1',3'-di-2-thienyl-5',7'-bis(2-ethylhexyl)benzo[1',2'-c:4',5'-c']dithiophene-4,8-dione)] (PBDB-T) is proposed as a potential donor for high voltage devices when paired with PCBM or $(3BS)_2$-SiPc. For reference, the molecular structures and energy levels for the four compounds are shown in Figure 4 and Figure 7.

The *J-V* plots for each device under 1,000 W/m^2 are shown in Figure 16, with the characteristics (power conversion efficiency (PCE), open circuit voltage (V_{OC}), short circuit current (J_{SC}), and fill factor (*FF*)) shown in Table 2. It is important to keep in mind that the device architecture was chosen to be simple and rudimentary to showcase the comparison between the active materials. Thus, the power conversion efficiencies and fill factors may be lower than those in devices from literature employing more complex designs.

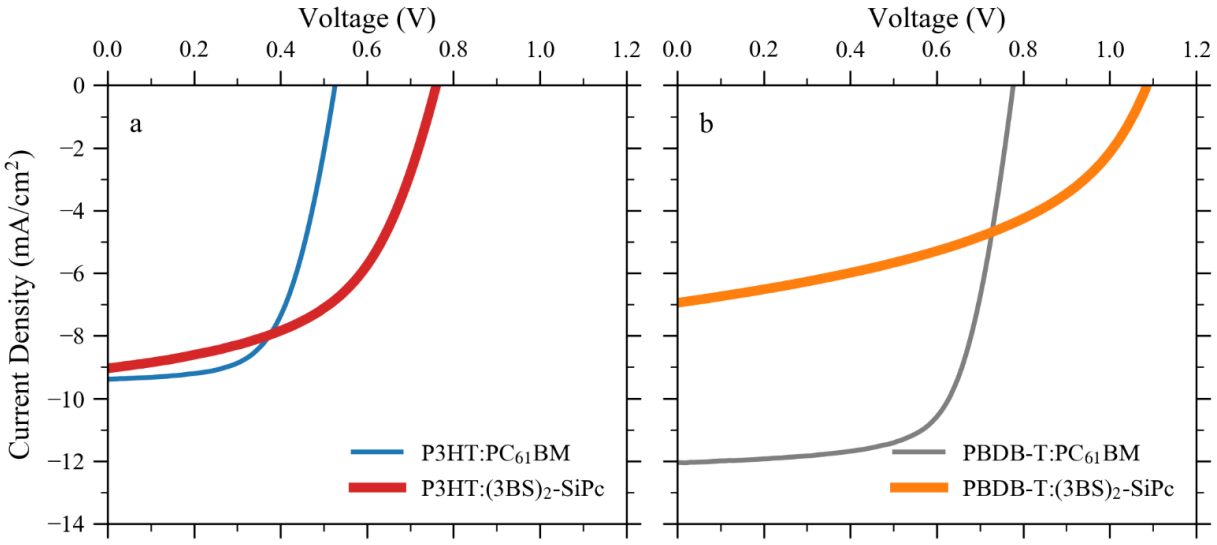

Figure 16: J-V curves for devices with the donor P3HT (left), and PBDB-T (right) (taken from [26]).

Table 2: Device performance extracted from J-V curves (taken from [26]).

Design	Donor	Acceptor	PCE (%)	V_{OC} (V)	J_{SC} (mA/cm^2)	*FF*
Reference 1	P3HT	$PC_{61}BM$	3.00 ± 0.06	0.53 ± 0.01	9.4 ± 0.4	0.61 ± 0.02
Design 1	P3HT	$(3BS)_2$-SiPc	3.6 ± 0.2	0.76 ± 0.01	9.0 ± 0.3	0.53 ± 0.02
Reference 2	PBDB-T	$PC_{61}BM$	6.4 ± 0.2	0.78 ± 0.02	12.1 ± 0.4	0.68 ± 0.01
Design 2	PBDB-T	$(3BS)_2$-SiPc	3.43 ± 0.09	1.09 ± 0.01	7.0 ± 0.3	0.45 ± 0.02

The two baseline devices, P3HT:PCBM and PBDB-T:PCBM, display comparable characteristics to similar devices in literature [51,52]. This shows that the results hereinafter were not due to improper baseline device fabrication.

It can initially be noticed that the P3HT:$(3BS)_2$-SiPc system has a greater PCE (3.6%) than that of P3HT:PCBM (3.00%), albeit with a lower FF (0.53 for the former, 0.61 the latter). The larger PCE arises

from the significantly larger V_{OC} (0.76 V) than that of the baseline P3HT:PCBM device (0.53 V), which was expected from the HOMO-LUMO difference of the donor:acceptor system. The two devices also retained a similar J_{SC} with one another (9.0 mA/cm^2 for the former, and 9.4 mA/cm^2 the latter). All these properties allude to the fact that the P3HT:$(3BS)_2$-SiPc system can compete, or even out-compete, the P3HT:PCBM system at 1,000 W/m^2 illumination.

The V_{OC}s of the two devices is an intrinsic behavior of the material systems, which is not expected to change much with device architecture. In this regard, the P3HT:$(3BS)_2$-SiPc system has an inherent advantage over the P3HT:PCBM one. However, the *FF* and J_{SC} may be increased through further optimized architecture or more modern designs. In one study, the PCE of a P3HT:PCBM system was increased from 4.3% to 5.5% while annealing at 140^{o}C, and in another work a P3HT:PCBM device was created with a large PCE of 6.82% [53,54]. Another way to increase these properties is to assess SiPcs with different axial group ligands, which will retain an almost identical V_{OC}, but may increase the *FF* and J_{SC} through morphological effects.

The external quantum efficiency (EQE) and absorption coefficient were measured as well, and shown in Figure 17a for the P3HT devices. The EQE for both devices show the same trend from approximately 400-650 nm, but with lower values for the P3HT:$(3BS)_2$-SiPc system. It is known through various studies in literature that the absorption of the P3HT:PCBM material system is mostly due to P3HT, except for in the UV range (approximately 300-350 nm), where absorption is through PCBM [55]. This is due to the absorbances of the respective compounds, which is related to the complex index of refraction, and seen in Figure 18 for reference. Thus, the similarities within the aforementioned range are not surprising. The lower EQE for P3HT:$(3BS)_2$-SiPc could be due to numerous reasons, but two reasons of suspect are the charge separation between donor and acceptor compounds, and charge transport in the acceptor. The HOMO-HOMO energy difference is smaller between P3HT and $(3BS)_2$-SiPc, which may decrease the efficiency due to a lower driving force. Also, the lower charge mobility in $(3BS)_2$-SiPc than PCBM may also contribute to a lower efficiency in this region. It is important to note that the EQE of the P3HT:$(3BS)_2$-SiPc system has a large peak around 350 nm, and extends further into the IR region than that of the P3HT:PCBM system. This is due to the large absorbance of $(3BS)_2$-SiPc within these regions. The larger EQE over the 650-725 nm range nearly makes up for the lower EQE over 400-650 nm, and allows for the statistically similar J_{SC} values for both devices.

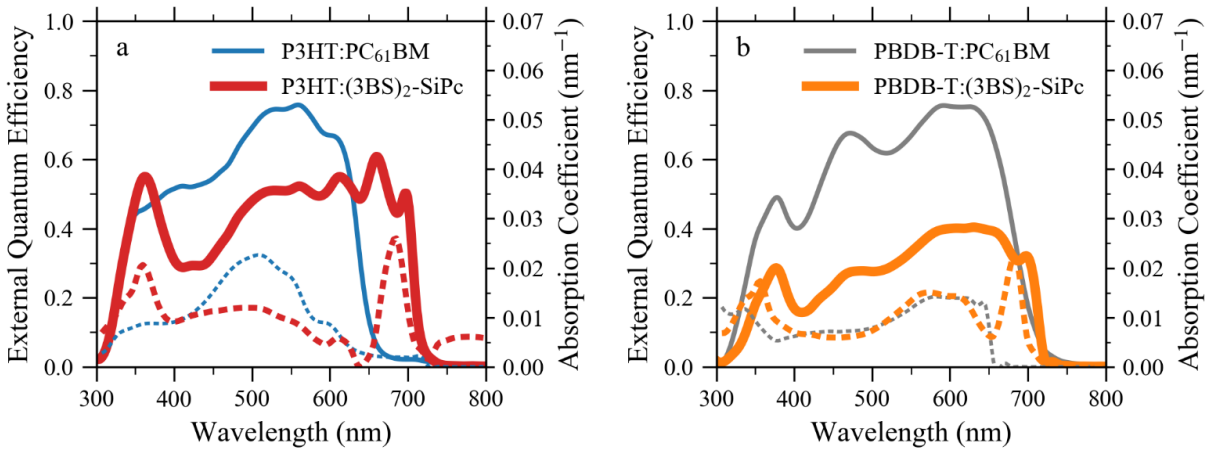

Figure 17: EQE (solid lines) and the absorption coefficient (dashed lines) for devices with the donor P3HT (left), and PBDB-T (right) (taken from [26]).

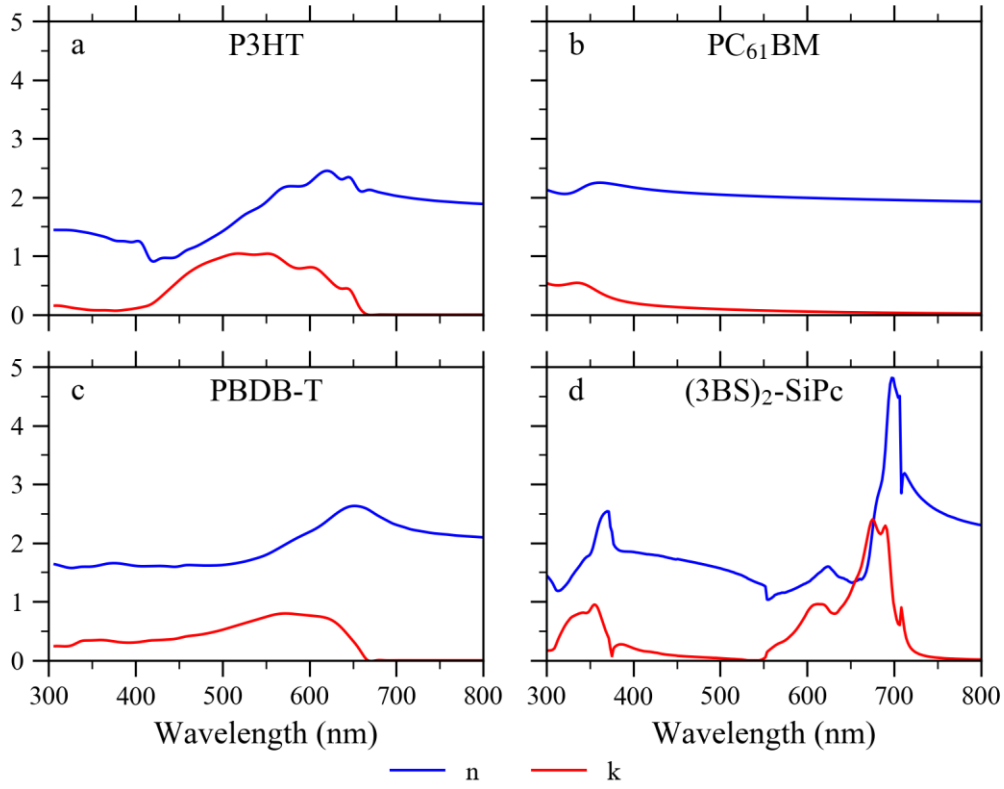

Figure 18: Optical parameters (n and k) for P3HT (a), PCBM (b), PBDB-T (c), and $(3BS)_2$-SiPc (d) (taken from [26]).

For the PBDB-T systems, the PBDB-T:$(3BS)_2$-SiPc blend has a lower PCE (3.43%) but larger V_{OC} (1.09 V) than PBDB-T:PCBM (6.4% and 0.78 V). This V_{OC} is on the larger side for OSCs, which may prove to be useful if the J_{SC} is able to be increased. However, as-is, the present PBDB-T:$(3BS)_2$-SiPc device does not

show a competitive design in comparison to other devices in literature, but showcases a V_{OC} among the largest of PBDB-T devices [56].

Looking at the EQE for the PBDB-T devices in Figure 17b, it can be seen that the PBDB-T:$(3BS)_2$-SiPc device has roughly half the efficiency as the PBDB-T:PCBM device. This is interesting, as the absorbances of the two systems are nearly identical, with exception to the $(3BS)_2$-SiPc peak near 700 nm. This is likely due to preferential absorption by PBDB-T over this range. As with the P3HT devices, this difference in efficiency may be due to a number of reasons, including charge separation and mobility. However, in the PBDB-T:$(3BS)_2$-SiPc blend, there is nearly no HOMO-HOMO energy gap, which lays the groundwork for very poor charge separation efficiency. As explained previously, the charge separation of the exciton is the key to OPV operation; it provides the voltage potential to drive the external circuit. The widely accepted minimum HOMO-HOMO gap for efficient charge generation is 0.3 eV, but can be lower through entropic driving forces, which could explain the phenomenon seen here [57]. For low energetic offset devices, it has been suggested that highly ordered donor and acceptor domains can lead to an increased *FF* and J_{SC} [58]. In future PBDB-T:$(3BS)_2$-SiPc devices, different morphologies of the active layer should be considered to increase the PCE.

As described in the experimental section, the new amorphous model was used to characterize the optical parameters of the materials, aside from P3HT, PBDB-T, and $(3BS)_2$-SiPc which used a point-by-point calculation. When characterizing the optical parameters for the blended active layer materials, it was treated as a single, uniform layer. The resulting optical parameters for the blends are shown in Figure 19, where it should be noted that an adequate fit could not be made for P3HT:$(3BS)_2$-SiPc in portions of the spectra. These portions of the P3HT:$(3BS)_2$-SiPc were important to include, as it is noticed that it possesses a lower absorbance than P3HT:$PC_{61}BM$ near 500 nm, but has a large absorbance peak from the SiPc acceptor near 700 nm. If we compare the optical parameters of the donor and acceptors to all of the blended materials, it can be seen that the blends show characteristics of their comprised compounds, as expected. In future work, this information may be used in optical and electrical models to optimize the active layer thickness.

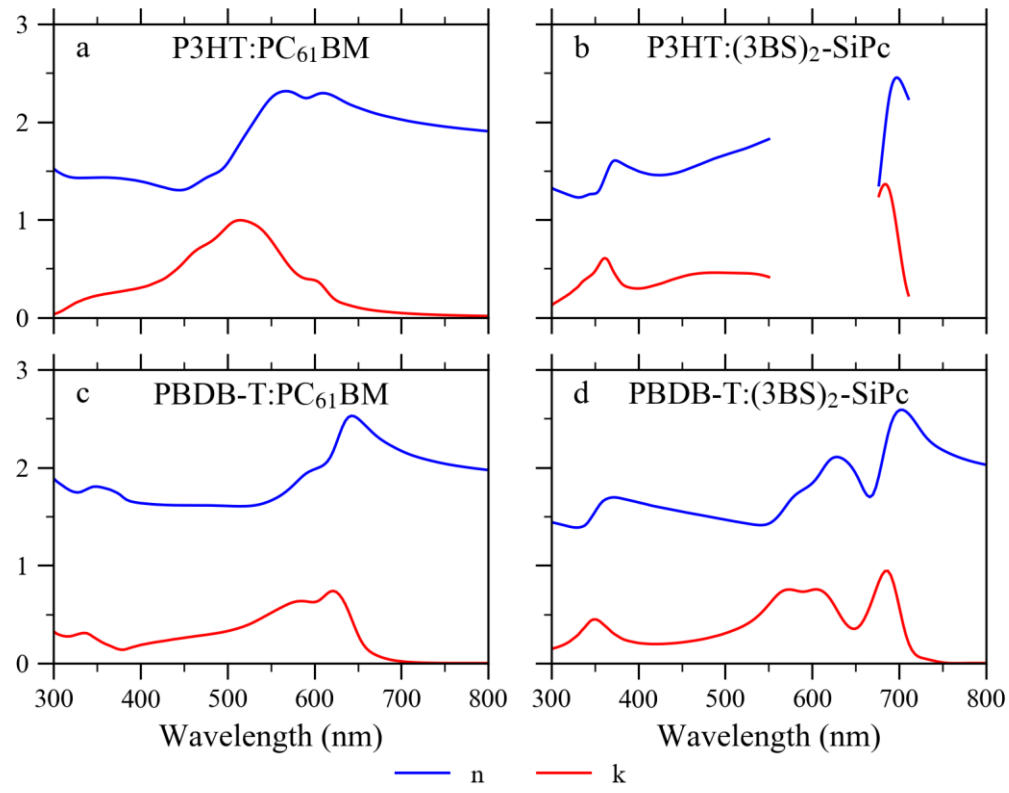

Figure 19: Optical parameters (n and k) for the active material blends P3HT:PCBM (a), P3HT:(3BS)$_2$-SiPc (b), PBDB-T:PCBM (c), and PBDB-T:(3BS)$_2$-SiPc (d).

3.2.2 Reduced Light Intensity

To further compare the devices, the characteristics were measured at reduced light intensities, from 800 W/m^2 to 5 W/m^2. The device characteristics (PCE, *FF*, V_{OC}, and J_{SC}) at various intensities is shown in Figure 20. It is interesting to see that the PCE initially rises with increasing intensity to approximately 200 W/m^2, after which it decreases for all devices. This appears to result from changes in the V_{OC}, where it increases logarithmically until approximately 200 W/m^2, then slightly deviates beneath this trend. This behavior can be explained through one of two effects, either the V_{OC} is reaching its saturation point, or leakage currents have skewed the *J-V* curve. As for the J_{SC}, it behaves as expected, and closely fits the power law with typical exponent values around 1 for organics [59].

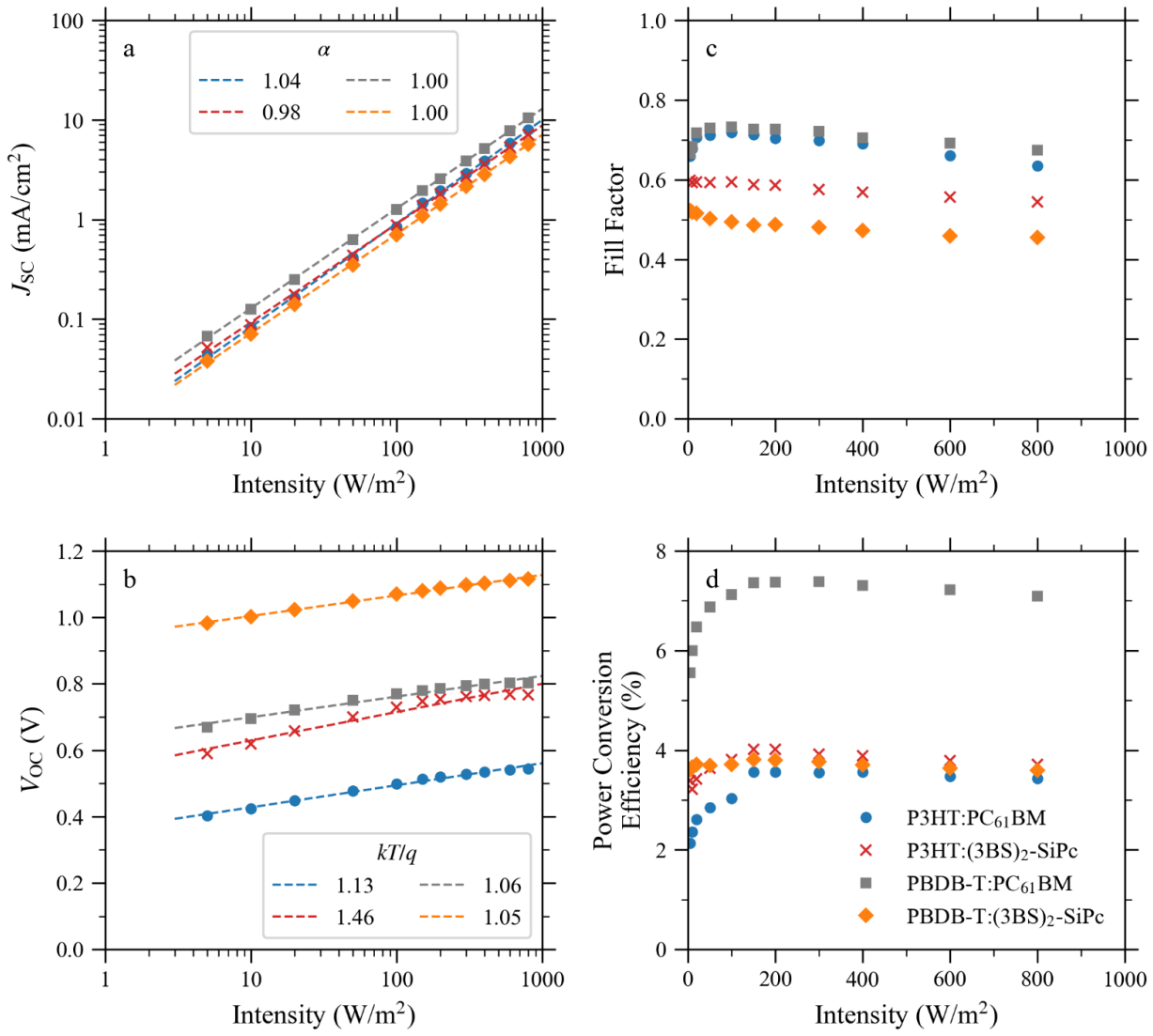

Figure 20: Device Characteristics under reduced light (taken from [26]).

In organic electronics, the V_{OC} has been shown to have a saturation point [60,61]. This is due to excess energy raising the energy level of the acceptor's LUMO, thus reducing the energy difference between the LUMO of the donor and acceptor. This energy difference decrease lowers the driving force for charge separation between the donor and acceptor which places an upper limit on the LUMO energy of the acceptor, and causes the observed saturation of V_{OC}. The V_{OC} values shown in Figure 20 start to taper off around 200 W/m^2, indicating that the saturation point has not yet been reached, but may be being approached. Conversely, this could also be explained through prominent leakage current effects at lower intensities [62]. It has been shown that devices with a low shunt resistance, <10^6 Ω cm^2, may

have skewed *J-V* characteristics due to parasitic leakage currents [62]. As seen in Figure 21, the measured shunt resistances fit this profile.

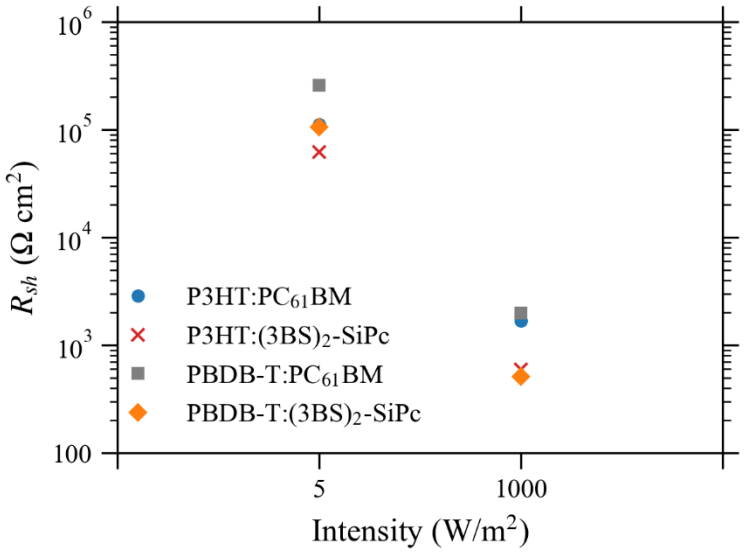

Figure 21: Shunt resistance of all devices at 5 W/m² and 1,000 W/m² (taken from [26]).

The V_{OC} was also assessed to understand the recombination effects within the OPV devices. Recombination losses are a strong contributor to a lower *FF*, so it is important to assess these to understand the loss mechanisms, and how to subsequently increase the *FF* [58]. The V_{OC} should have a logarithmic relation with increasing intensity, with a slope of kT/q, where k is the Boltzmann constant, T is the temperature in Kelvin, and q is the elementary charge. A slope of 1 represents a system with only bimolecular recombination, and a slope greater than 1 represents trap-assisted recombination [62]. Trap-assisted recombination is not ideal, as the additional recombination pathway leads to a decreased *FF* [63]. As mentioned previously, the slope of the *J-V* relation may be skewed due to leakage current or saturation effects. The authors of the study state that the determination of bimolecular and trap-assisted recombination is more difficult in this situation, since the low shunt resistance will increase the V_{OC} slope at low intensities. Therefore, the types of recombination cannot be precisely determined here. However, qualitative information may be gained through an assessment of these features. It can be seen from Figure 20 that the PBDB-T:(3BS)$_2$-SiPc device strongly correlates with bimolecular recombination over the entire range of intensities. However, the other devices display elements of trap-assisted recombination at lower intensities, which is common in literature [64]. This indicates that the *FF* may be increased by reducing the amount of trapped states in the devices.

Regardless of leakage current effects, there are some other qualitative pieces of information we can gain from the *FF* analysis. A decrease in *FF* with increasing light intensity is consistent with recombination effects, since recombination is proportional to the charge carrier concentration. This effect is observed for all devices, except for PCBM containing devices under 100 W/cm^2. For these, an increase of *FF* with increasing light intensity is consistent at these low concentrations due to more prominent leakage current effects.

The charge mobilities within the active layer materials can also influence the *FF*. A larger charge mobility allows for faster extraction from the device, resulting in less recombination. From Figure 20 it can be seen that the $(3BS)_2$-SiPc containing devices have a lower *FF* than with PCBM, as expected with a the lower mobility in $(3BS)_2$-SiPc. The *FF* can be effected by other phenomenon, such as contact limitations, high degree of mixing in the blend, and geminate recombination (charge pairs that have not escaped their Coulomb interaction) [58]. These can be explored further in future work for increased device performance.

3.2.3 Angle Dependence

The angular dependence of the devices were also assessed. This assessment is important for OSCs, as many applications will involve incidence light at oblique angles, such as fixed-tilt solar harvesting devices, and applications that exploit the flexibility of OSCs. The PCE at various angles of incidence are shown in Figure 22 for all devices. The trends for the PBDB-T devices are similar between the two acceptors, where the PCE increases with the angle of incidence until a specific point, then decreases. In literature, this increase has been attributed to an increased optical path length and a modified interference pattern within the active layer at larger angles of incidence, while the decrease arises from increasing amounts of reflection from the air-glass interface [65]. Contrary to this, the P3HT devices display the same increase, but do not decrease, even at the highest measured angle of incidence. When comparing the angle dependence of the acceptor compounds, $(3BS)_2$-SiPc displays a larger increase in PCE than PCBM in the P3HT blend, while displaying a less pronounced increase and decrease than PCBM in the PBDB-T blend.

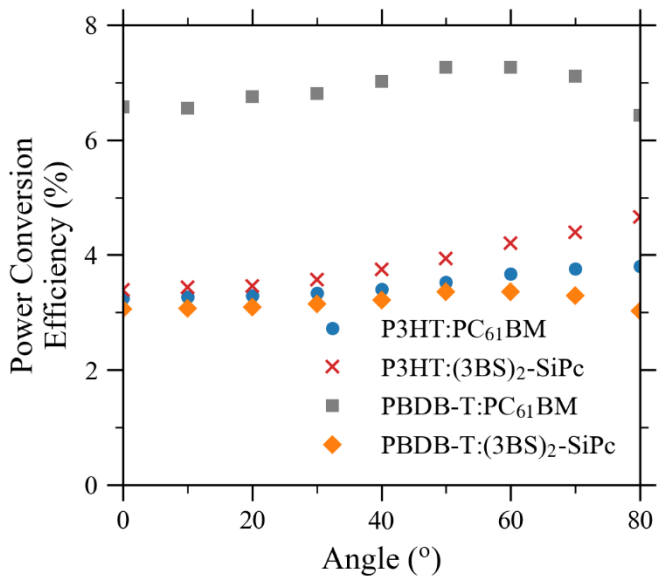

Figure 22: Angle dependence of the PCE for all devices at 850 W/m² (taken from [26]).

To further study the device characteristics the different angles of incidence, the PCE, *FF*, V_{OC}, and J_{SC} were plotted as functions of intensity while accounting for cosine losses at each angle, since the behavior under reduced light intensities has previously been determined. The angle dependent characteristics were taken at three different intensity levels of the experimental apparatus, corresponding to 850, 500, and 250 W/m² at normal incidence, and are displayed in Figure 23. It should be noted that reflection losses become more prominent with a larger angle of incidence but were not accounted for in the data set, and this should be taken into consideration when reading into these results.

It can be seen that the *FF* and V_{OC} appear to vary independent of the angle of incidence, and follow similar trends as at reduced intensity levels. However, the V_{OC} values increase less with intensity than expected, almost at half the rate as with reduced intensity at normal incidence, and the P3HT:PCBM device displayed almost no net change at the extremities of the measurements. This will have a considerable positive impact on the PCE with decreasing angle of incidence, but the cause of this phenomenon was not identified due to the complexity of open-circuit voltage in organic solar cell devices.

As for the J_{SC}, it does not follow a linear trend with intensity for each device. Rather, it deviates in a concave fashion from the trend with a maximum around 40-50°, irrespective of the intensity. This can be seen in Figure 24, which displays the difference between the J_{SC} and the linear regression of the J_{SC}

values at normal incidence. Irrespective of the initial intensity, each set of angular experiments displays the same trend, except for the P3HT:$PC_{61}BM$ blend at 850 W/m^2.

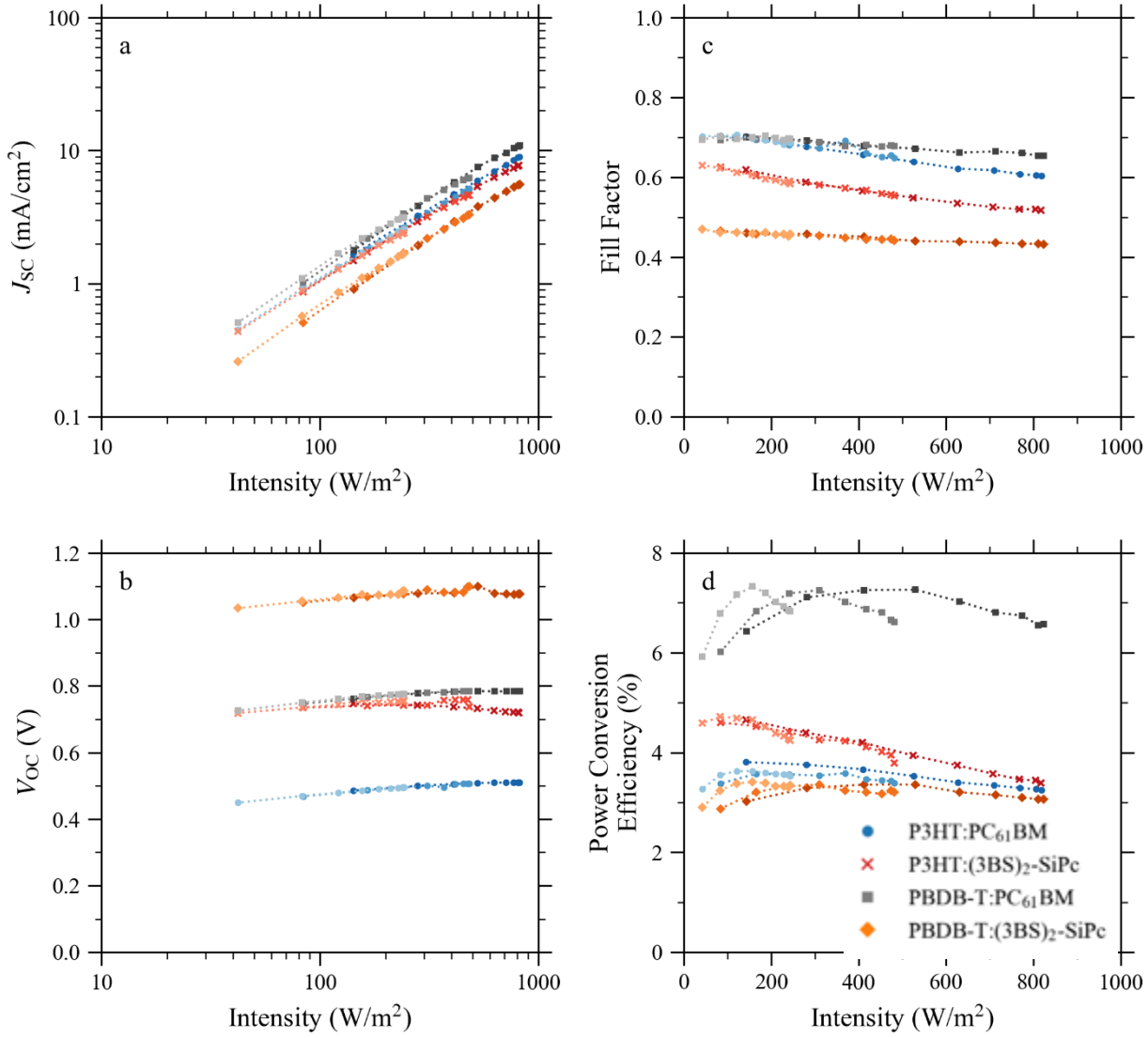

Figure 23: Device Characteristics at various angles of incidence for normal incidence intensities of 850, 500, 250 W/m^2, and plotted as a function of the associated intensity measured through cosine losses.

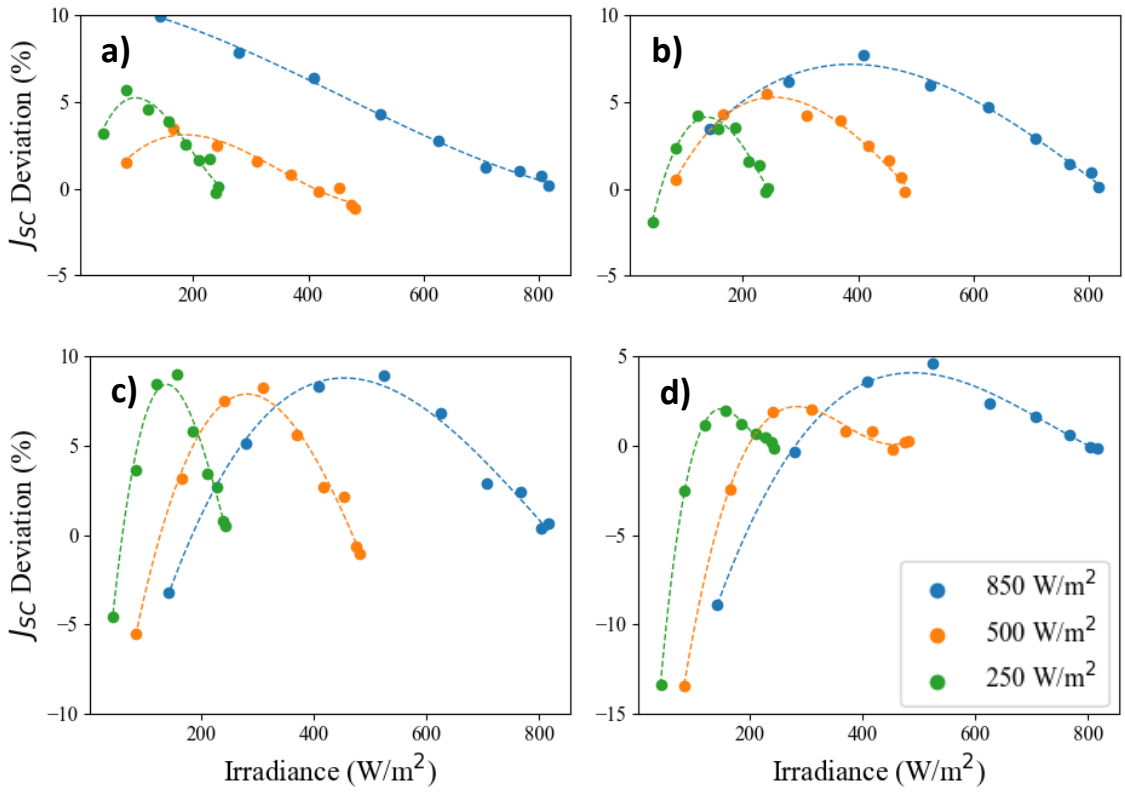

Figure 24: J_{SC} deviations from each incidence angle to that of normal incidence at identical light intensity for P3HT:PC_{61}BM (a), P3HT:$(3BS)_2$-SiPc (b), PBDB-T:PC_{61}BM (c), and PBDB-T:$(3BS)_2$-SiPc (d). Irradiance listed in the legend represent the intensity at 0° incidence for each series.

The PCE behavior of the devices at various angles can be largely be explained through this trend in J_{SC}. Both trends display the same concave nature when plotted against light intensity. As mentioned previously and which will be explained in more detail in the following section, the increase in J_{SC} arises from an increased optical path length and a modified interference pattern, and the decrease in J_{SC} arises from an increase in reflection losses. This is why the PCE is seen to increase, then decrease with the angle of incidence in the PBDB-T devices. The P3HT devices were not always shown to have a decrease in PCE, but this can be explained through the small magnitude of the J_{SC} deviation at larger angles of incidence.

3.2.4 Wavelength Dependences and Modelled Absorbance Profiles

For further investigation into the BHJ active layers, EQE measurements were taken to determine the wavelength dependent behavior. This was done at various angles of incidence in order to further explain the results from the angle dependent studies.

The EQE for all devices at several angles of incidence are shown in Figure 25. The curves are blue-shifted with increasing angles of incidence, which is consistent with literature [65]. This shift was confirmed through an absorbance model of the OSC devices, where the absorbance within the active layer was simulated at various angles of incidence with coherent irradiation, and displayed in Figure 26 for $PC_{61}BM$ containing devices. Similarly to other works in literature, the blue-shifted absorbances decrease with increasing angle of incidence, with more significant changes occurring past 60°.

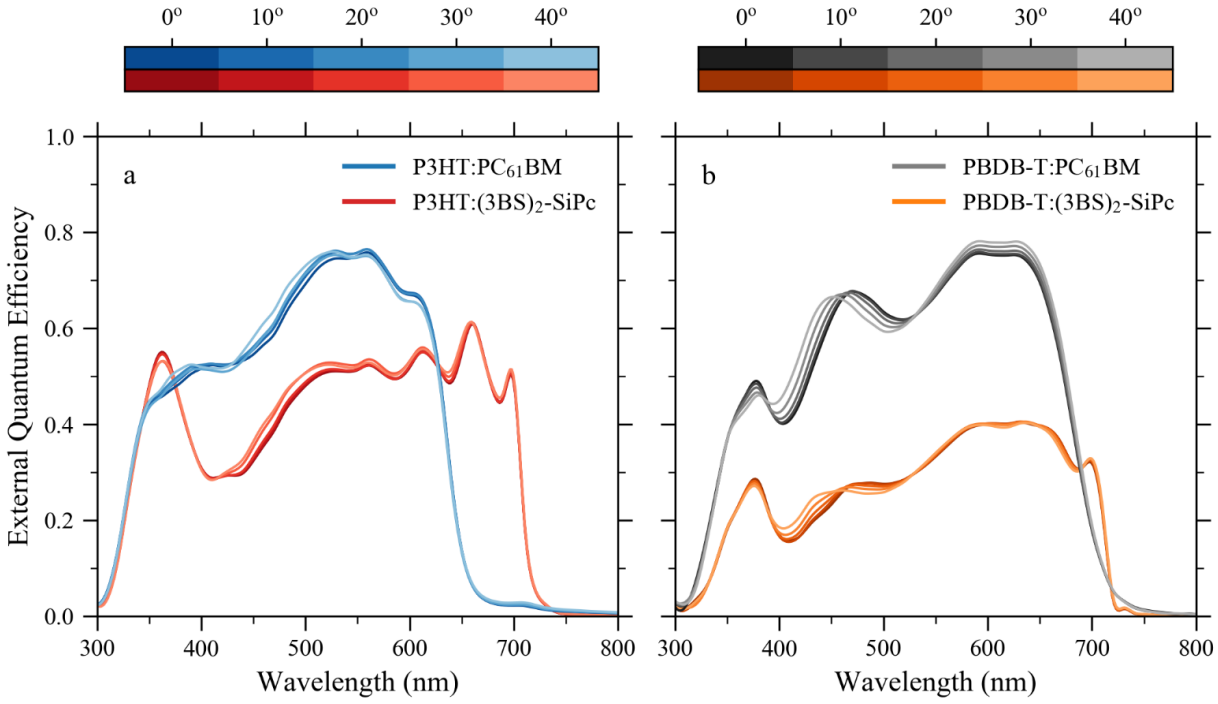

Figure 25: Angle dependence of the experimentally measured external quantum efficiency for all devices (taken from [26]).

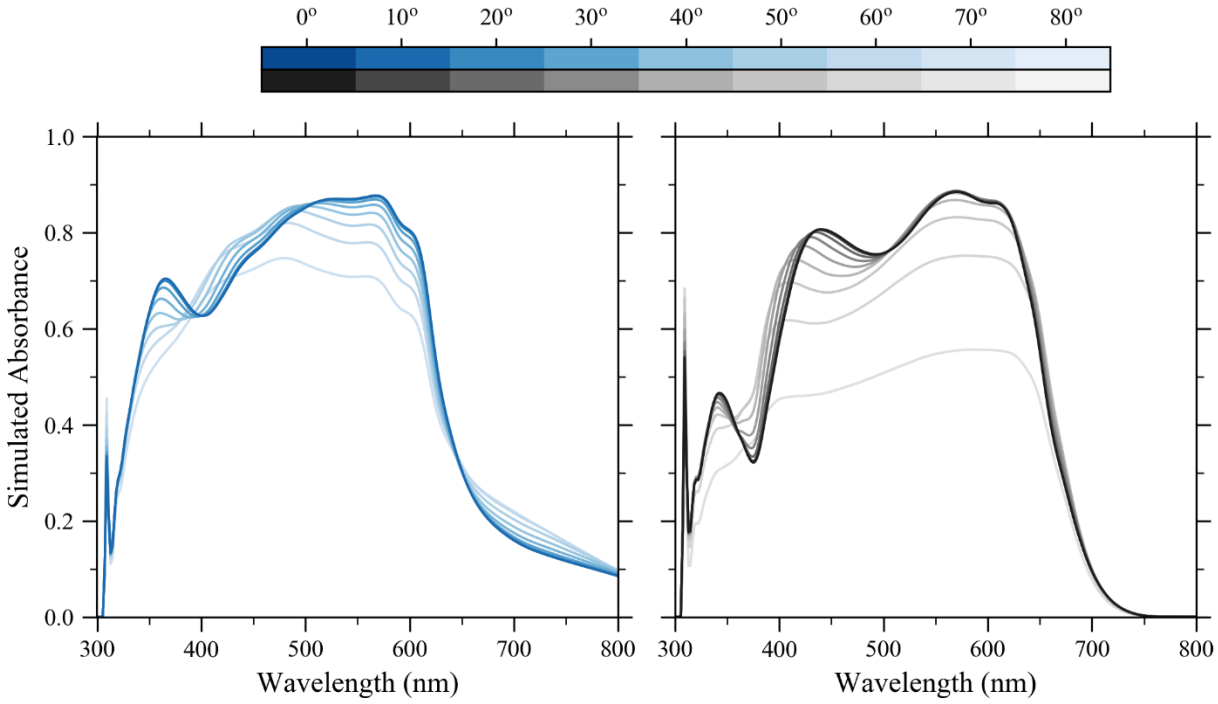

Figure 26: Simulated active layer absorption using an optical model in Solcore for $PC_{61}BM$ devices with coherent irradiation for P3HT:$PC_{61}BM$ (left) and PBDB-T:$PC_{61}BM$ (right) devices.

It can readily be seen that for P3HT:$PC_{61}BM$ there is an increase in absorbance around 450-500 nm, and a decrease in absorption around 575-625 nm. This is consistent with the EQE spectra in Figure 25, where the increase in absorption corresponds to an increase in EQE, and vice versa. The PBDB-T:$PC_{61}BM$ device has a similar behavior, where there is an increase in absorbance from around 350-425 nm, and two decreases just below 350 nm and around 425-500 nm. This is consistent with the device's EQE, except that the EQE also increases with the angle of incidence from approximately 500-700 nm, but the total absorbance within this region remains the same. However, this may be explained through the absorbance profile of the device, shown in Figure 27, where it was seen that excitons at 40° incidence are formed closer to the top of the layer than at normal incidence, near the ITO contact [65].

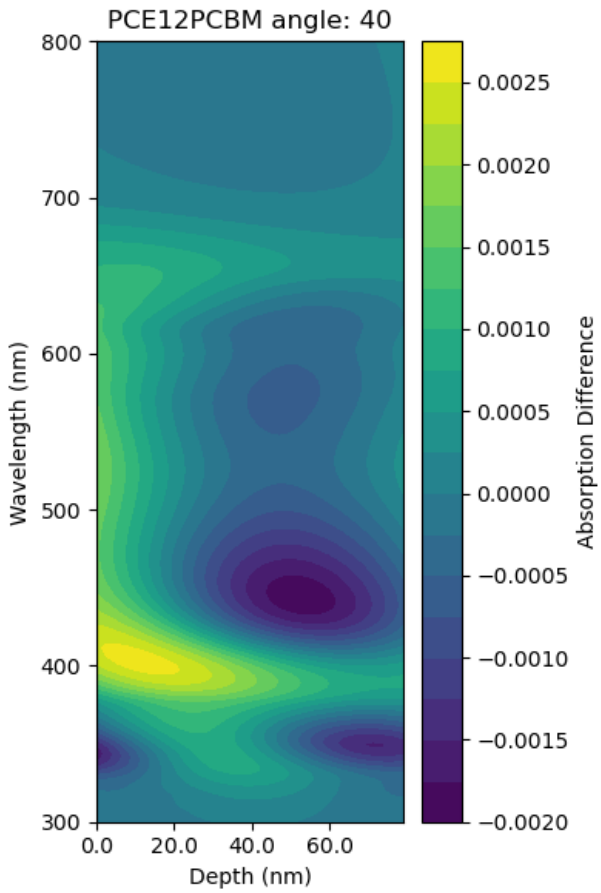

Figure 27: Simulated absorbance difference profile for coherent absorption in the PBDB-T:$PC_{61}BM$ device, where the difference between absorption at 40° and 0° incidence is shown.

Due to the similar behavior between $PC_{61}BM$ and $(3BS)_2$-SiPc devices, the following analyses in this section were done on the $PC_{61}BM$ devices as more accurate optical parameters were obtained. The previous absorbances were calculated with coherent irradiation, as the EQE apparatus displayed coherency. In operation, solar cells are exposed to incoherent solar radiation, so the absorbance as a function of wavelength under incoherent irradiation was simulated. The results for the $PC_{61}BM$ devices can be seen in Figure 28.

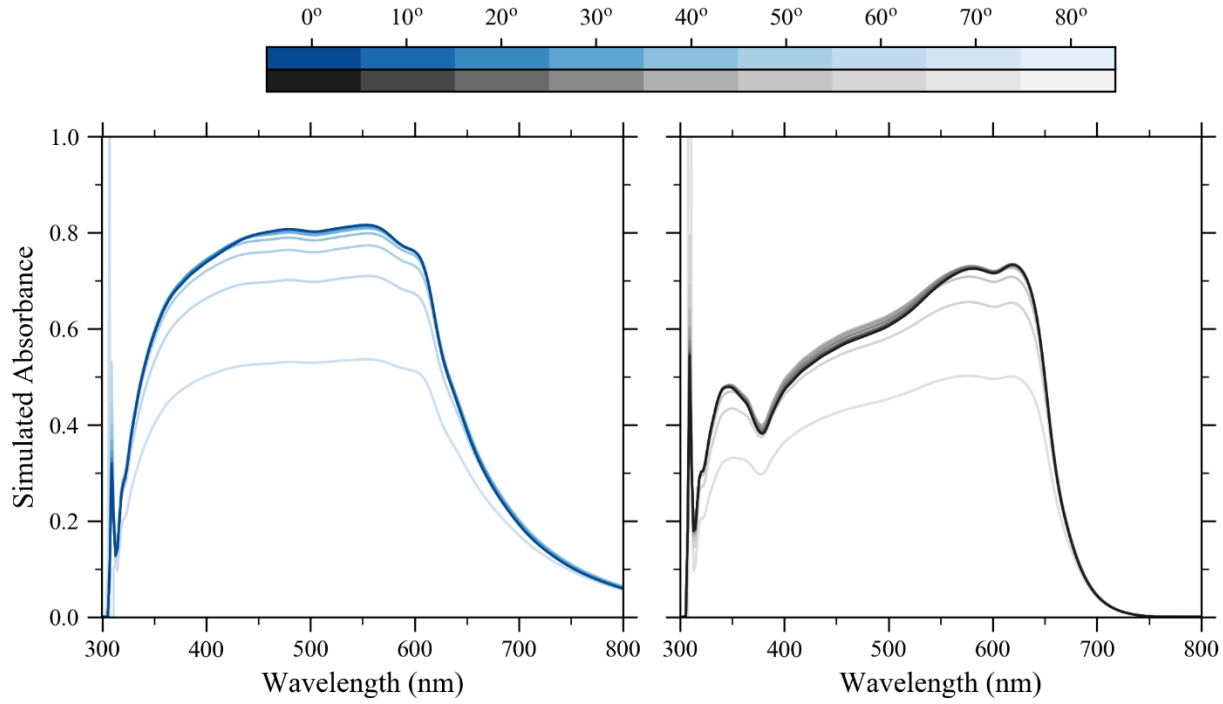

Figure 28: Simulated active layer absorption using an optical model in Solcore for $PC_{61}BM$ devices with incoherent irradiation for P3HT:$PC_{61}BM$ (left) and PBDB-T:$PC_{61}BM$ (right) devices.

It is immediately noticed that contrary to the EQE for coherent absorption, there is no blue-shift trend of the absorbance. However, the overall absorbance appears to be similar in magnitude until approximately 60°, where the absorbance profile decreases in magnitude significantly at all wavelengths.

As for minor deviations of the EQE, the P3HT:$PC_{61}BM$ device visually appears to have little increase in absorbance with increasing angle, but it is apparent that the PBDB-T:$PC_{61}BM$ device has an increase in absorbance between 400-550 nm. Through the integral of the product of this absorbance profile with the AM1.5G spectra, the total absorbed current at each angle of incidence can be estimated. When plotted as a function of light intensity, the absorbed power displays the same concave nature as in the angle dependent J_{SC} plots. In order to display this, the difference between the absorbed power at a given angle and the absorbed power at 0° incidence at the same intensity was taken. The simulated total absorbed power, and the percent increase from normal incidence as a function of angle for the $PC_{61}BM$ devices is shown in Figure 29.

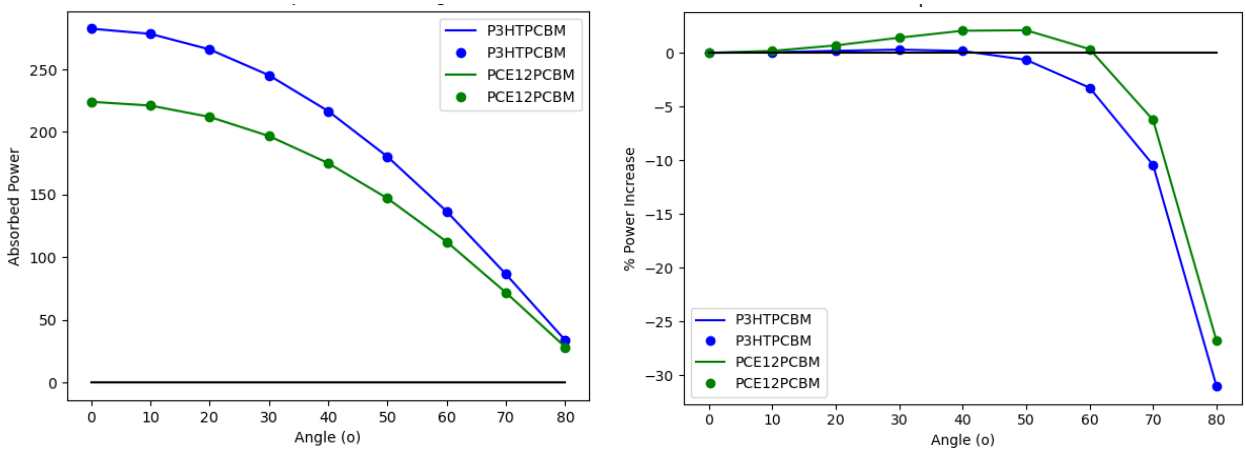

Figure 29: Simulated absorbed power at each angle of incidence (left), and the power increase in comparison to normal incidence at the same intensity (right).

A small positive deviation is initially found for the devices, which is indicative of the larger optical path-length at larger angles of incidence. Likewise, the negative deviation at larger angles is indicative of increasing reflective losses from the system. These both support the J_{SC} behavior in the angle dependence study, especially the PBDB-T devices, where the peak in J_{SC} occurs at a similar location as predicted through the absorbed power simulation. This is not the case for the P3HT devices, and other phenomena may be occurring in these devices to offset the reflective losses in the system.

4 Chapter IV: Photonic Power Converters

Chapter 4 discusses the work performed with photonic power converters. Section 4.1 details the architecture of the multijunction devices, and the optoelectronic methods used within the Solcore models. Section 4.2 contains the results and discussion of the three different device architectures used, and exemplifies the importance of light trapping effects within photonic power converters.

Additional information regarding contact fabrication on semiconductor wafer parts is also discussed within section 4.1. Although indirectly related to the rest of the chapter, this comprised a substantial amount of work done throughout this thesis project in a supportive role within a larger team.

4.1 Experimental

4.1.1 Photonic Power Converter Design

A GaAs PPC with 5 junctions was used to demonstrate the implementation of light-trapping effects with a back-reflector. The architecture of the device was taken to mimic that of a PPC reported in literature, without a reflective surface [66]. For this, each junction is comprised of a front surface field, emitter, base, back surface field, and a tunnel junction. The absorber used for the emitter and base is GaAs, which provides operation at a design wavelength of 835 nm. The surface fields consist of n- and p-doped GaInP layers, and each junction is connected by an AlGaAs tunnel diode. The architecture of each junction in the PPC can be seen in Figure 8, and the entire 5-junctions can be seen in Figure 9. The absorbing layer thicknesses of the PPC were determined through the Beer-Lambert Law at 835 nm, and can be seen in Table 3. This structure was implemented into Solcore for analysis [10].

Table 3: Thicknesses of the absorbance matched GaAs PPC with five junctions.

JUNCTION	THICKNESS
1	214.9 nm
2	276.1 nm
3	386.8 nm
4	651.3 nm
5	2955.5 nm

4.1.2 Optical and Electrical Modelling

The optical performance of the simulated PPCs were determined using the transfer matrix method. As with the prior modelling of organic solar cells, the "tmm" software package in Python was used for the TMM method [46].

The input spectrum of light, which represented a laser source, uses a Gaussian distribution with a mean of 835 nm and a standard deviation of 2 nm. After which, the absorbance profile as a function of depth within the simulated solar cell could be attained, and the electrical properties calculated using the depletion approximation.

4.1.3 Contact Fabrication

In addition to modelling, I also contributed to the fabrication of experimental devices. The experimental processes performed will be described herein, but no analysis or discussion will be shown. This work has contributed to several publications [67–69].

The photonic power converters were manufactured as a collaboration through the University of Waterloo, and the University of Ottawa. The InAlGaAs semiconductor growth was done at the University of Waterloo with molecular beam epitaxy on a p-doped InP substrate, then sent to the University of Ottawa for metallization and testing. Metallization was done at the NanoFab, which is part of the Centre for Research in Photonics at the University of Ottawa, except for the metal deposition of the back contact, which was done at the National Research Council (NRC). A summary of the top and bottom contact compositions can be seen in Table 4.

Table 4: Photolithography spin coating steps.

	Bottom Contact	**Top Contact**
Composition	Au	Au 50 nm
	Pd	Pd 15 nm
	Zn	Ti 15 nm
	Pd	Pd 9 nm
	InP	**InGaAs**
Post-Treatment	400 °C	
	2 minutes	

The composition of the top contact, Pd/Ti/Pd/Au, was chosen because it offered an ohmic contact that could be fabricated in-house at the University of Ottawa [70–72]. For this design, the bottommost Pd layer was used to adhere to the wafer to form a low-resistive metal-semiconductor interface. The following Ti and Pd layers are then used to form a diffusion barrier and an ohmic contact, with the top Au layer providing a large sheet conductivity. The design of the bottom Pd/Zn/Pd/Au contact was similar, but Zn was used instead of Ti as the second layer. The annealing process allowed Zn to diffuse into the bottommost Pd layer, which created the low-resistive interface with InP.

The bottom contact was fabricated first, due to an annealing step following metal deposition. Initially, the native oxides on the InP substrate were removed through a 2 minute immersion in a 12% (v/v) HCl solution. Unless otherwise stated, following chemical treatments, such as in this step, the wafers were rinsed with deionized water and dried with compressed nitrogen. The wafers were then sent to NRC for metal deposition, where a thin layer of SPR-955 photoresist was spin coated on the top surface to prevent scratches in the PVD chamber. At NRC, PVD was used to sequentially deposit Pd, Zn, Pd, and Au with their confidential recipe [73]. Upon their return to the University of Ottawa, the photoresist was dissolved and devices cleaned with successive immersion in acetone, isopropanol, and deionized water. The contact was then annealed in a Solaris 100 rapid thermal annealer at 400^{o}C for 2 minutes, and cooled under nitrogen.

A Pd/Ti/Pd/Au metallic contact was used to connect to the top surface of the device, an n-doped InGaAs cap layer. Photolithography was used for patterning, and PVD for metal deposition. The surface was initially prepared with a successive cleaning cycle through immersion in acetone, isopropanol, and deionized water. The sample was then heated at 180^{o}C for 5.0 ± 0.1 minutes on a hot plate to remove residual moisture. A Microchem LOR-1A lift-off layer, followed by a Megaposit SPR 955-CM photoresist layer, were spin coated onto the semiconductor using the steps outlined in Table 5. An OAI Model 204IR mask aligner with a 350 watt I-line near-UV lamp was used for UV exposure, using a custom soda-lime photolithography mask with chrome patterning. Samples were exposed at 85 mJ/cm^2, then developed in Dow MF-CD-26 for 35 seconds. An Angstrom Nexdep physical vapor deposition machine was then used to sequentially deposit Pd, Ti, Pd, and Au. Lift-off was done through immersion in Microchem Remover PG. Finally, the sample was cleaned through sequential immersion in acetone, isopropanol, and deionized water, then dried with compressed nitrogen. As a final step, the InGaAs cap layer was removed with a selective wet etch down to the InAlAs etch stop layer. A solution with a 1:2 volumetric

ratio of H_2O_2 to 50 wt% citric acid was pre-mixed, then the devices were immersed for 3.0 ± 0.1 minutes at room temperature [74,75].

Table 5: Photolithography spin coating steps.

	Microchem LOR-1A		**Megaposit SPR 955-CM**	
Spin Time	45	seconds	15	seconds
Spin Speed	3000	RPM	6000	RPM
Annealing Time	5.0 ± 0.1	minutes	3.0 ± 0.1	minutes
Annealing Temperature	180	°C	100	°C

Transfer length measurements (TLM) were performed with custom patterns to measure both the top and bottom contact resistances, and were found to be suitable for use in experiments.

Two images of photovoltaic devices that were fabricated with the aforementioned top contact in the NanoFab at uOttawa are displayed in Figure 30 [69]. These devices were fabricated to test an InAlGaAs tunnel diode within a 2-junction PPC. In the published work, the epitaxial growth temperatures were studied to determine the effect on the junction's peak tunneling current density. A large peak tunneling current density is beneficial, as this value must be larger than the current density travelling through a PPC during operation. The study showed that a reduction of 20°C from the original growth temperature caused a 10^3-10^4 % improvement in peak tunneling current. This allowed for peak tunneling current densities larger than 1200 A/cm^2, which can be useful for PPCs capturing 100 W/cm^2 of optical power. Further results on this and similar projects can be found in Meghan N. Beattie's Ph.D. thesis, which will be published in 2021.

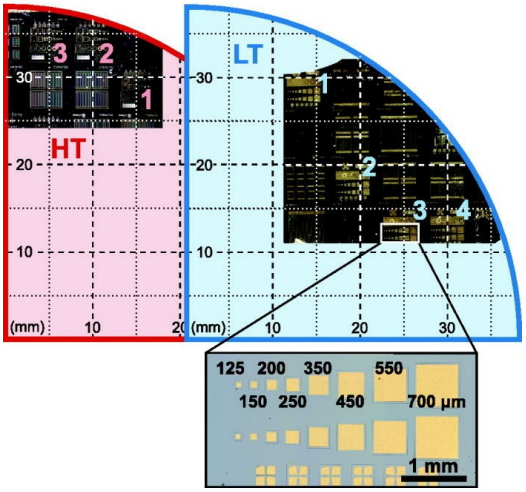

Figure 30: Top view microscope images of photovoltaic devices containing InAlGaAs tunnel diodes, including a close-up image of the contact pads used for current-voltage measurements. Reproduced from [69], with the permission of AIP Publishing.

4.2 Modelling Results and Discussion

4.2.1 No Reflector

The 5-junction PPC was simulated initially with the five junctions on a GaAs substrate as an absorption matched device. This represents a typical device, epitaxially grown on a substrate, where an electrode is deposited beneath the substrate. The current-voltage (*I-V*) and external quantum efficiency (EQE) curves can be seen in Figure 31 and Figure 32.

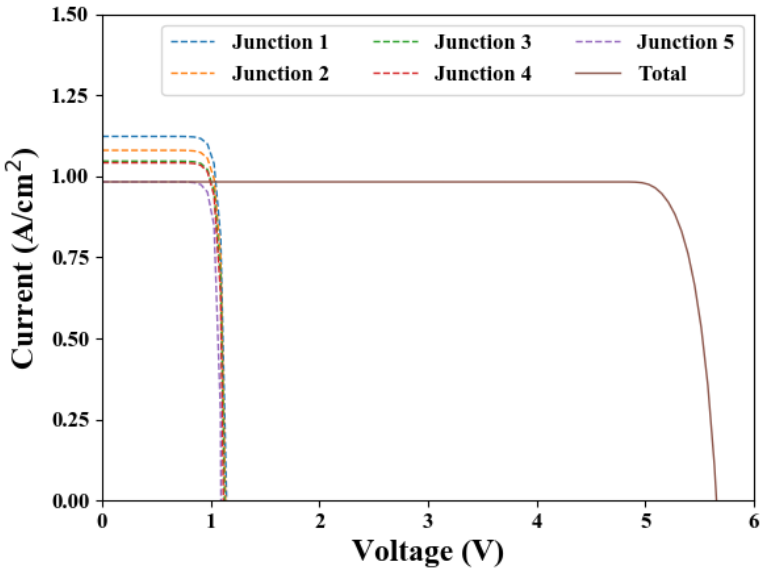

Figure 31: I-V plot for the 5-Junction GaAs PPC.

When designing PPCs, it is desirable to have a current-matched device, where all junctions output the same amount of current. As seen in Figure 31, each junction has a similar short-circuit current density (J_{SC}). The discrepancy between the J_{SC} values of the junctions indicates that optimization of the PN junction thicknesses can be done. The PN junction thicknesses were chosen based off the Beer-Lambert Law, which estimates the thickness required for equal absorption, not equal current generation. For a current matched device, the junction efficiencies, which decrease with increasing thickness and decreasing light intensity, must be taken into account. As seen by the EQE in Figure 32, the EQE of each junction is approximately the same near the midpoint of the laser source spectrum at 835 nm, shown in Figure 33, but not identical. The larger junctions have lower efficiencies, which cause them to output less current than the top junctions under the same absorbance. Even under perfect optimization, this restriction will remain in place. However, if a reflective surface is placed beneath the last junction, the thicknesses of the lower junctions can be significantly decreased, and allow for increases in efficiency.

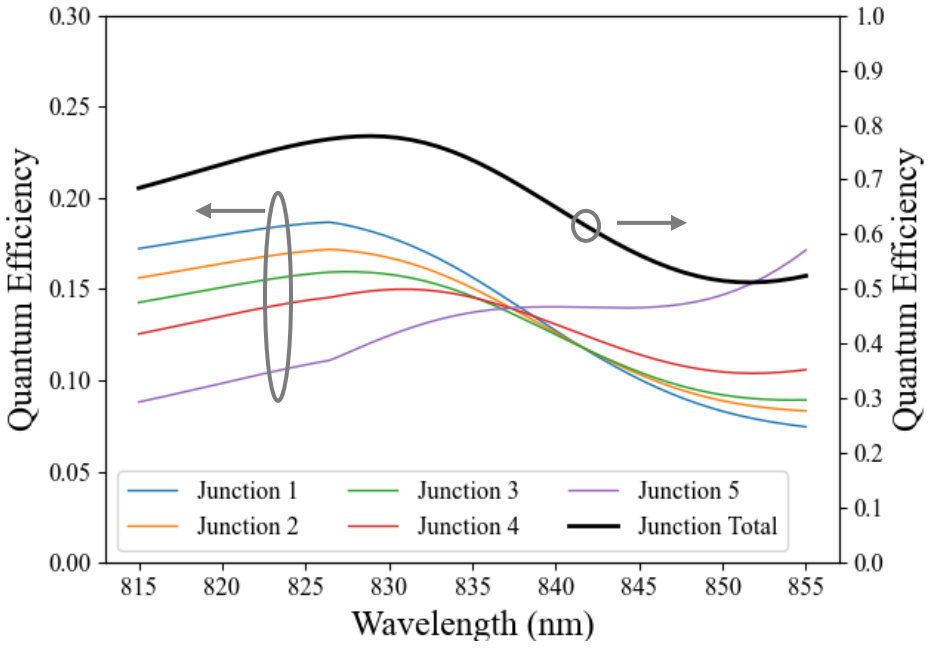

Figure 32: The external quantum efficiency of each junction within the 5-junction PPC.

In an ideal PPC, the total quantum efficiency at the design wavelength would be close to the design target, which is 99% here. The total quantum efficiency within the simulated PPC in Figure 32 is lower than this value. A phenomena that was not accounted for within the simulated PPCs is luminescent coupling. This occurs when light emitted from radiative recombination is absorbed within a different

junction, which increases the current within the re-absorbing junction. When a junction absorbs more light than it can convert into a current, the excess energy is primarily re-emitted through radiative recombination [66]. Since the junctions within the simulated PPC in this work are not perfectly current-matched with one another, a large degree of radiative recombination can be expected. Luminescent coupling was not modelled, and the energy lost by radiative recombination effects were taken to be lost by the system. This effect could contribute to the low quantum efficiency shown in Figure 32.

Another challenge with PPC design arises from a non-uniform absorption coefficient, as shown in Figure 33 for GaAs. In this scenario, the absorption coefficient is larger for wavelengths below 835 nm, and smaller above this wavelength. As seen in Equation (2.4), the absorbance for a fixed thickness of absorbing material is related to its absorption coefficient, where a larger value causes a greater absorption. If the top-most junction of a multijunction PPC absorbs more than the design amount, then the junctions below it receive a lower intensity of light and absorb less than they would otherwise. In this manner, a larger absorption coefficient for the device causes the upper junctions to absorb more light, and the bottom junctions to absorb less. The opposite occurs for a smaller coefficient. The junctions within the PPC were designed for a target wavelength of 835 nm, and due to the non-uniform absorbance parameter of GaAs around this wavelength, the aforementioned phenomenon causes the shape of the EQE curves in Figure 32 to occur. Similarly, the choice of light source can also have an effect on the current matched properties of the PPC device by distributing power at wavelengths further from the design target. Due to all the aforementioned complexities within PPC design, the use of machine learning for optimization of junction thicknesses could be considered due to the complexity of the parameter space.

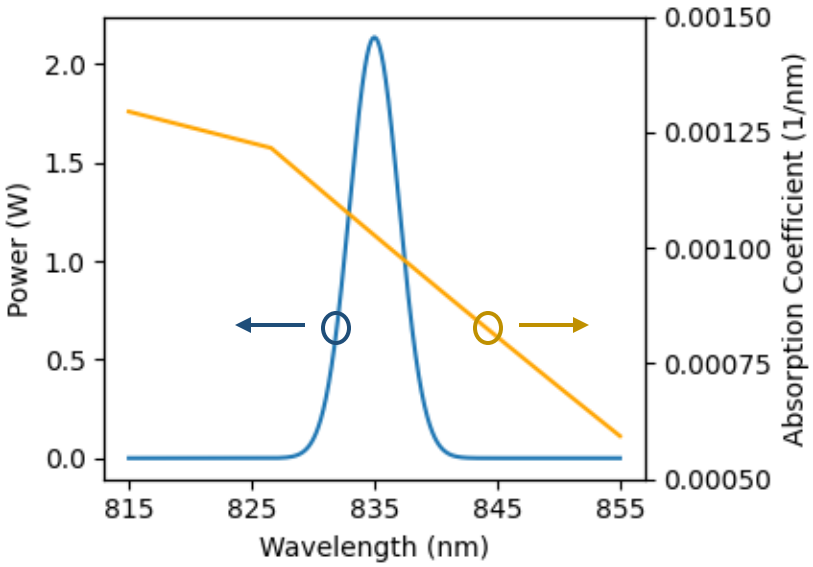

Figure 33: The power spectrum of the laser (blue), and the absorption coefficient for GaAs (yellow).

To demonstrate the effect of a reflective surface implemented in a multijunction PPC, two different PPC architectures were simulated. These included a PPC without a reflective surface (PPC-A), and with a reflective surface while only changing the 5th junction's thickness (PPC-B). These architectures are displayed in Figure 34, where the characterization of PPC-A was previously demonstrated.

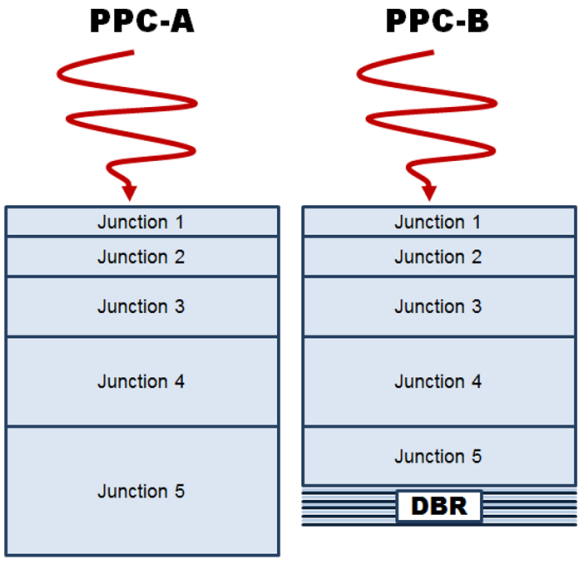

Figure 34: Relative junction thicknesses of PPC-A (left) and PPC-B (right). PPC-A does not include a reflective surface at the rear, while PPC-B does, which results in a lower thickness (and higher efficiency) of junction 5 (taken from [76]).

4.2.2 Metallic Reflector

For initial simulations for a reflector for the PPC, a metallic layer was used. Since a metallic layer is required for PPC operation, this offers a low-complexity approach for light management. However, if an absorbing substrate is used for the PPC, it must be removed before contact deposition, such as with the aforementioned lift-off technique. Assuming such an approach can be used with the simulated five junction PPC, the resultant PPC architectures PPC-B-MT (PPC-B with a metallic reflector) was demonstrated. Initially, to determine the thickness of a silver contact required for reflectivity, the reflectivity of the contact as a function of thickness was simulated. As seen in Figure 35, a metallic thickness of 100 nm is sufficient to allow for maximum reflectivity by this reflector, and is used for the subsequent simulations.

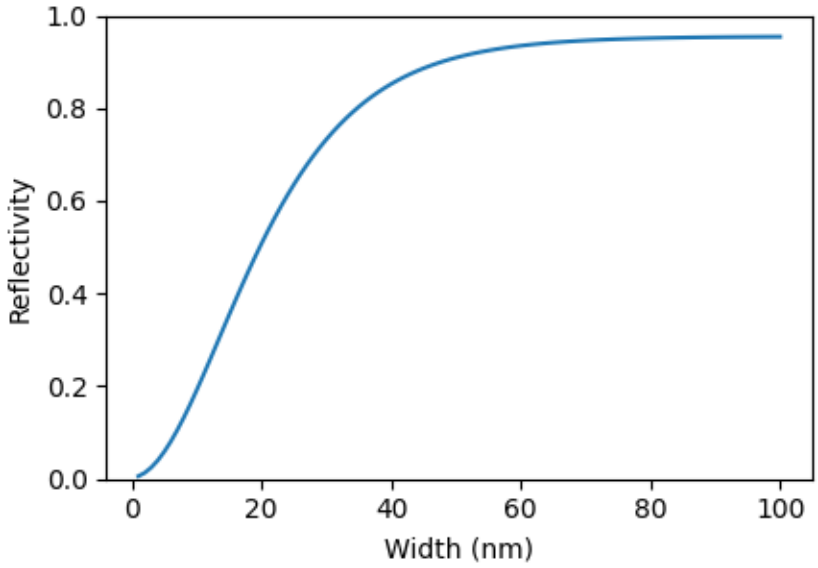

Figure 35: Reflectivity of a layer of silver, with maximum reflectivity at approximately 95.4%.

A simulation for PPC-B-MT was then performed to determine the thickness of the 5th junction required. For this, a silver layer of 100 nm was added to the rear of PPC-A, and the current density within junction 5 simulated as a function of its thickness. Figure 36 shows these results, where three items can be noticed. Initially, at the largest thickness, the incorporation of the metallic reflector allows for an increase in current density, which is expected due to the larger absorbance in light. While the junction thickness decreases, the current density increases slightly. This contributes to the increase in quantum efficiency with a decrease in junction thickness, as less recombination losses occur with a thinner junction. Following this increase, the current density finally decreases due to lower absorption, and

eventually falls below that of the benchmark, PPC-A. The minimum thickness of junction 5 retaining a current density greater than PPC-A was found to be 1058 nm, as depicted in Figure 36. The oscillations observed are due to modelled sharp interfaces in thin layers. For fabricated devices, interfaces are not as sharp, and therefore these oscillations may not be observed.

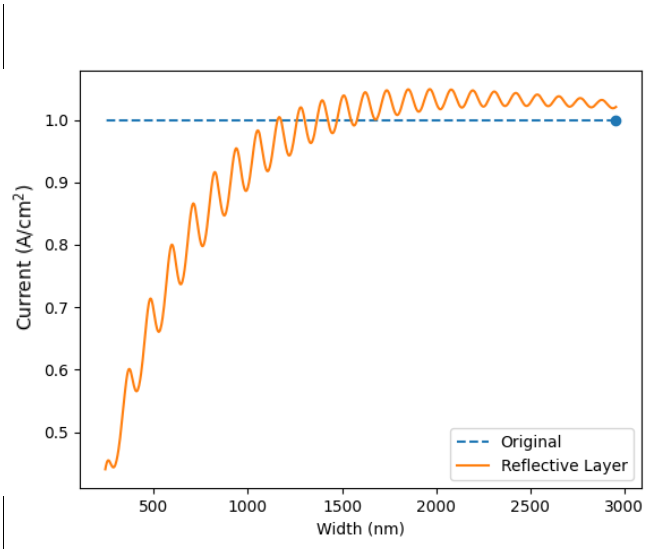

Figure 36: Current density of PPC-B-MT as a function of the thickness of junction 5. The original current density of PPC-A is indicated at a thickness of 2955 nm.

A PPC with a metallic reflector and a thinner 5th junction at 1058 nm offers the same current density with a junction thickness of 2955 nm and without the reflector, while maintaining the top 4 junction thicknesses. This can have practical benefits for current matched purposes between the 5 junctions. As discussed previously, a difficulty with designing a current-matched PPC arises from the non-linear relationship of junction efficiency with junction thickness, where the lower junctions are more difficult to match. The incorporation of the reflector at the rear of the device allows for more light absorption within the layer, and can increase current output. This is a way to prevent the last junction from limiting the current of the entire device. As shown previously in Figure 31, PPC-A has a mismatch of current densities between the different junctions, with the limiting junction being the 5th junction. Raising the current density of this junction will cause a direct improvement on the entire PPC's performance, as shown in Figure 37 when comparing PPC-A and PPC-B-MT. It can be noticed that the inclusion of a metallic reflector in PPC-B-MT allows for an increase in current density for the entire device.

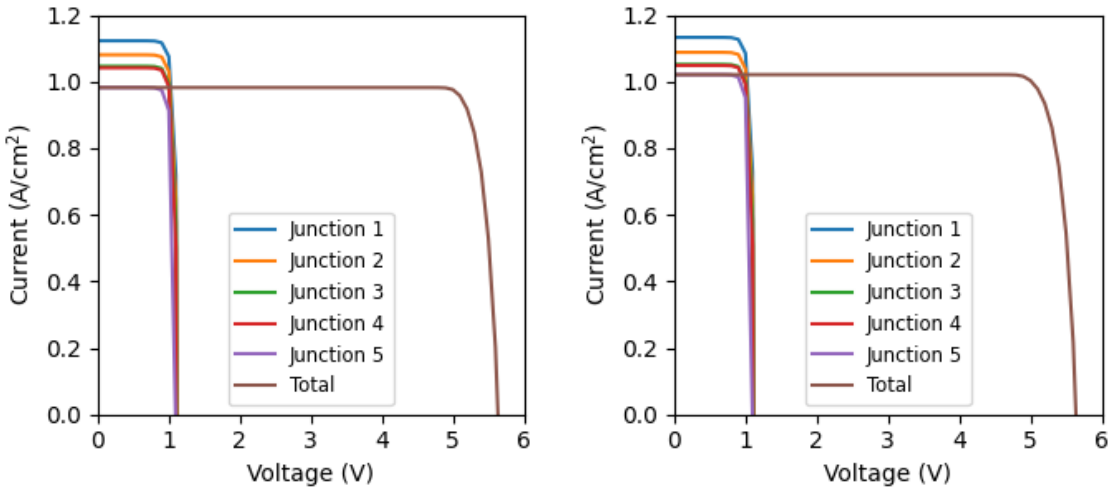

Figure 37: Comparison of the simulated I-V relationships of PPC-A (left) and PPC-B-MT (right).

4.2.3 Distributed Bragg Reflector

A DBR was also simulated as a reflective surface for the PPC. The DBR was placed between the substrate and the fifth junction. Alternating layers of AlAs and $Al_{0.3}Ga_{0.7}As$ were used as the DBR. The choice of AlAs and $Al_{0.3}Ga_{0.7}As$ were made, as they can be lattice matched with the GaAs substrate, and that the materials exhibit low absorption at 835 nm. The indices of refraction of AlAs and $Al_{0.3}Ga_{0.7}As$ at 835 nm are 3.0 and 3.4, respectively. The advantage of using a DBR instead of a metallic reflector is that a DBR can be incorporated directly with the growth of the PPC, while a metallic reflector must be placed after a post-growth lift-off process.

For this design, the thicknesses of the AlAs and $Al_{0.3}Ga_{0.7}As$ layers, in addition to the number of repeating layers, were required for optimization. The initial conditions for the DBR thicknesses were taken to be a quarter wavelength stack (61.2 nm for AlAs, and 72.3 nm for $Al_{0.3}Ga_{0.7}As$), and an optical simulation was done to determine the number of repeating layers. As seen in Figure 38, 40 repeating layers provides a reflectivity near unity. This high number may be impractical for implementation, so a value of 10 repeating layers was chosen for the simulations, which offers a reflectivity of 63%. A different choice in DBR materials with a larger index of refraction difference may offer higher reflectivity with a lower amount of repeating layers.

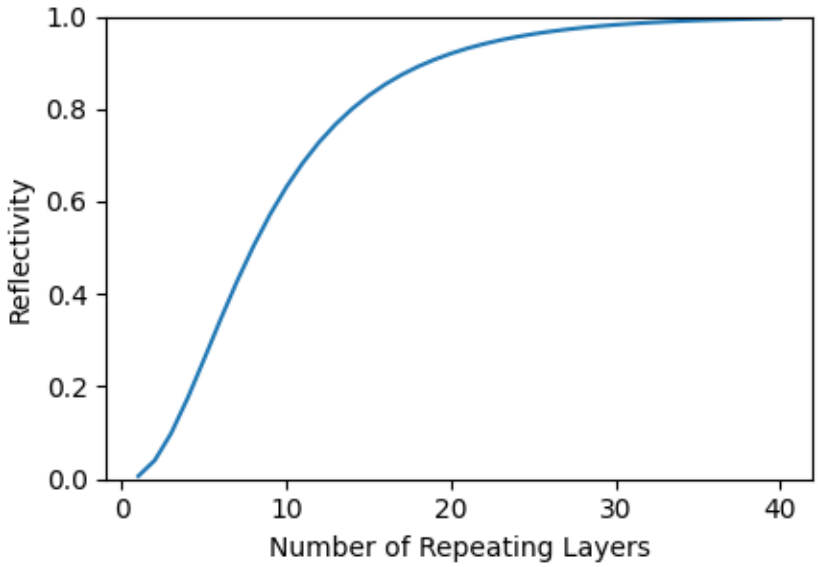

Figure 38: Reflectivity of a distributed Bragg reflector with various multiples of repetitive layers.

The optimization for the 5th junction and DBR in PPC-B-BR (PPC-B with a Bragg reflector) was then performed. Initially, a DBR layer was added to the device PPC-A following the 5th junction, and before the substrate. An iterative process was then used to determine the thickness of the base layer in junction 5, then the thicknesses of the alternating layers in the DBR. The objectives of these processes were to minimize the thickness of the base layer within the 5th junction while maintaining the same short circuit current density as PPC-A, and to determine the thicknesses of the DBR layers to maximize the quantum efficiency within the 5th junction. The results of the final iteration of the optimization can be seen in Figure 39 for the DBR thicknesses, and in Figure 40 for the 5th junction thickness.

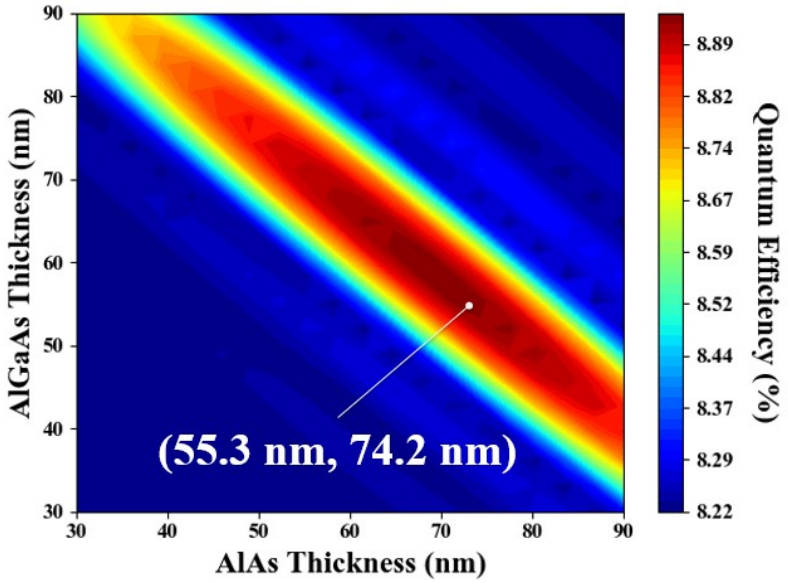

Figure 39: Optimization of the thicknesses of AlGaAs and AlAs layers in the DBR stack.

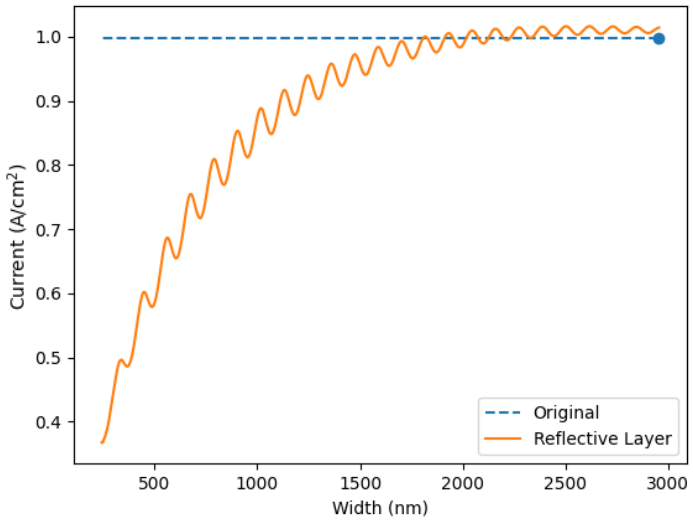

Figure 40: Current density of PPC-B-BR as a function of the thickness of junction 5. The original current density of PPC-A is indicated at 2955 nm.

As seen by Figure 39, the thicknesses of the DBR layers (55.3 nm for AlAs, and 74.2 nm for $Al_{0.3}Ga_{0.7}As$) differ slightly from the initial guess of the quarter wavelength stack (61.2 nm for AlAs, and 72.3 nm for $Al_{0.3}Ga_{0.7}As$). However, the quantum efficiency of the 5th junction is similar between these two solutions, and a quarter wavelength stack could be used without much loss in efficiency. Figure 40 shows that the thickness of the 5th junction can be decreased from 2955 nm to 1710 nm with the

incorporation of the aforementioned reflector, while still retaining the same current density. This relation closely resembles that of PPC-B-MT, albeit with a lesser effect from the DBR due to reflection losses. Additionally, it is important to note that the reflectivity of the DBR is sensitive to deviations of the wavelength and in layer thicknesses, whereas the metallic reflector is less sensitive to these effects. For these reasons, the metallic reflector may be more advantageous to incorporate within a PPC design.

5 Chapter V: Conclusions

Two photovoltaic systems were discussed within this thesis. Organic solar cells, and photonic power converters. The open-source software package Solcore was used to model and aid in the analysis of optoelectronic properties of both systems.

Solar energy is an important resource to capture to transition away from non-renewable energy sources. Organic solar cells are a type of solar cell that have relatively low cost manufacturing costs and with the potential for fast payback periods. Bulk heterojunction solar cells are a typical organic solar cell design, where donor and acceptor compounds are blended together to form the active layer. In this study, the acceptor $(3BS)_2$-SiPc is assessed in a blend with P3HT for a potentially competitive alternative to the conventional P3HT:PCBM blend, and in a second blend with PBDB-T for a high V_{OC} device.

Photonic power converters are photovoltaic devices which convert optical power into electrical power. These have applications in the telecom industry to provide power over fiber, in addition to other select applications that can exploit the electrical isolative and electromagnetic resistive properties of such systems. Multijunction photonic power converters are often used for increased operating voltages and efficiencies. To further improve upon these efficiencies, the incorporation of both a metallic and distributed Bragg reflector at the rear of a device was demonstrated and analyzed.

5.1 Organic Solar Cells

In these studies, we compared the performance of organic solar cells containing the phthalocyanine derivative $(3BS)_2$-SiPc to those containing the more common acceptor PCBM. The benefits of using $(3BS)_2$-SiPc include lower synthetic costs due to a two-step chemical synthesis with ease of purification, and modifiable physical properties for solution processing. These were prepared in bulk heterojunction blends with P3HT, which is the preferred reported donor for commercialization in the future. A second donor, PBDB-T, was also used as a donor to achieve a high V_{OC} device due to low energetic offsets.

Devices with the P3HT:$(3BS)_2$-SiPc blend had a PCE of 3.6%, which is larger than that of the baseline P3HT:PCBM device at 3.0%. This was due to a larger V_{OC} of 0.76 V in comparison to 0.53 V for P3HT:PCBM, where both devices had similar *FF*s and J_{SC}s. The PBDB-T:$(3BS)_2$-SiPc device achieved a large V_{OC} of 1.09 V, but with a PCE of 3.4% in comparison to the PBDB-T:PCBM device PCE of 6.4% at 0.78 V. The PCE of the PBDB-T:$(3BS)_2$-SiPc device may be improved with further optimization of both the axial ligands, film morphology, and active layer thickness to improve both the *FF* and J_{SC}. The $(3BS)_2$-SiPc containing devices both showed an increase in PCE under reduced light intensities, resulting from lower

recombination rates. These devices also displayed superiority over PCBM containing devices over various angles of incidence, where the P3HT device displayed greater increases in PCE, and the PDBD-T device displayed decreased sensitivity to angles of incidence. Due to the greater performance of the P3HT:$(3BS)_2$-SiPc device over P3HT:PCBM at 1,000 W/m^2, reduced light intensities, and various angles of incidence, the phthalocyanine derivative $(3BS)_2$-SiPc deserves further investigation as a potential acceptor for commercialization.

5.2 Photonic Power Converters

The incorporation of reflective surfaces at the rear of a multijunction photonic power converter were demonstrated in modelling. A 5-junction GaAs PPC was used for this, with the incorporation of metallic, and distributed Bragg reflector. The Beer-Lambert law was used for absorbance matching for absorbing layer thicknesses. This demonstrated adequate current matched properties between layers for an initial estimate for the device design. The incorporation of a reflector at the rear of the device allowed for the thinning of the bottom junction, which caused an increase in efficiency. Partial thinning of the bottom junction allowed for an increase in absorption, which assisted in increasing the overall PPC's power output. The metallic reflector was deemed to be more advantageous over the distributed Bragg reflector, as it allows for a higher reflectivity with less wavelength dependance.

5.3 Optoelectronic Simulations with Solcore

The open-source optoelectronic software package Solcore was used to simulate both organic solar cells and PPCs for separate projects. The organic solar cells were previously fabricated and had experimental data available. Using Solcore's optical solvers, simulations were done to aid in the analysis of the experimental datasets, and further understand the behavior of the material systems of interest. On the other hand, the PPCs were simulated entirely using Solcore using materials with well-known properties. We studied light management techniques and concluded that a metal reflector can be more advantageous than a DBR design. The results may aid in future design processes for the architecture and fabrication of physical PPCs.

5.4 Future Steps

Future work for the organic solar cells could involve the comparison of P3HT:$(3BS)_2$-SiPc and P3HT:PCBM blends within updated device architectures than those fabricated in this work, along with the study of other silicon phthalocyanine acceptors. Additionally, optoelectronic simulations can be done to estimate layer thicknesses to aid in the design of the solar cells. This would require various optical and

electrical properties of the blends to be measured, such as carrier mobilities and recombination rates, along with the optical parameters measured within this work.

For the photonic power converters, future work on this project could include the analysis of different light trapping techniques, such as textured surfaces for the scattering of light, and using artificial intelligence to aid in the design of current matched multijunction PPCs.

6 References

1. BP, "Statistical Review of World Energy," (2020).
2. H. Ritchie and M. Roser, "Energy," Our World in Data (2014).
3. A. Louwen and W. van Sark, "Chapter 5 - Photovoltaic solar energy," in *Technological Learning in the Transition to a Low-Carbon Energy System*, M. Junginger and A. Louwen, eds. (Academic Press, 2020), pp. 65–86.
4. Y. Huang and C. K. Luscombe, "Towards Green Synthesis and Processing of Organic Solar Cells," The Chemical Record **19**, 1039–1049 (2019).
5. J. E. Carlé, M. Helgesen, O. Hagemann, M. Hösel, I. M. Heckler, E. Bundgaard, S. A. Gevorgyan, R. R. Søndergaard, M. Jørgensen, R. García-Valverde, S. Chaouki-Almagro, J. A. Villarejo, and F. C. Krebs, "Overcoming the Scaling Lag for Polymer Solar Cells," Joule **1**, 274–289 (2017).
6. A. Anctil, E. Lee, and R. R. Lunt, "Net energy and cost benefit of transparent organic solar cells in building-integrated applications," Applied Energy **261**, 114429 (2020).
7. "Organic Photovoltaics on Greenhouse Rooftops: Effects on Plant Growth," Materials Today: Proceedings **19**, 65–72 (2019).
8. C. E. Valdivia, M. M. Wilkins, B. Bouzazi, A. Jaouad, V. Aimez, R. Arès, D. P. Masson, S. Fafard, and K. Hinzer, "Five-volt vertically-stacked, single-cell GaAs photonic power converter," in *Physics, Simulation, and Photonic Engineering of Photovoltaic Devices IV* (International Society for Optics and Photonics, 2015), Vol. 9358, p. 93580E.
9. M. N. Beattie, M. M. Wilkins, M. C. Tam, C. E. Valdivia, and Z. R. Wasilewski, "Optical Characterization of InAlGaAs on InP for Monochromatic Photonic Power Conversion," in *2019 Photonics North (PN)* (2019), Vol. CFP1909V-ART, pp. 1–1.
10. D. Alonso-Álvarez, T. Wilson, P. Pearce, M. Führer, D. Farrell, and N. Ekins-Daukes, "Solcore: a multi-scale, Python-based library for modelling solar cells and semiconductor materials," J Comput Electron **17**, 1099–1123 (2018).
11. Yen-Yi Lin, D. I. Gundlach, S. F. Nelson, and T. N. Jackson, "Pentacene-based organic thin-film transistors," IEEE Transactions on Electron Devices **44**, 1325–1331 (1997).
12. S. Ya-Rui, W. Hui-Ling, S. Ya-Ting, and L. Yu-Fang, "Theoretical study of the charge transport mechanism in π-stacked systems of organic semiconductor crystals," CrystEngComm **19**, 6008–6019 (2017).
13. J. C. S. Costa, R. J. S. Taveira, C. F. R. A. C. Lima, A. Mendes, and L. M. N. B. F. Santos, "Optical band gaps of organic semiconductor materials," Optical Materials **58**, 51–60 (2016).
14. K. Gao, L. Li, T. Lai, L. Xiao, Y. Huang, F. Huang, J. Peng, Y. Cao, F. Liu, T. P. Russell, R. A. J. Janssen, and X. Peng, "Deep Absorbing Porphyrin Small Molecule for High-Performance Organic Solar Cells with Very Low Energy Losses," J. Am. Chem. Soc. **137**, 7282–7285 (2015).
15. T. Xia, Y. Cai, H. Fu, and Y. Sun, "Optimal bulk-heterojunction morphology enabled by fibril network strategy for high-performance organic solar cells," Sci. China Chem. **62**, 662–668 (2019).
16. H. Yin, S. H. Cheung, J. H. L. Ngai, C. H. Y. Ho, K. L. Chiu, X. Hao, H. W. Li, Y. Cheng, S. W. Tsang, and S. K. So, "Thick-Film High-Performance Bulk-Heterojunction Solar Cells Retaining 90% PCEs of the Optimized Thin Film Cells," Advanced Electronic Materials **3**, 1700007 (2017).
17. Y. Tong, Z. Xiao, X. Du, C. Zuo, Y. Li, M. Lv, Y. Yuan, C. Yi, F. Hao, Y. Hua, T. Lei, Q. Lin, K. Sun, D. Zhao, C. Duan, X. Shao, W. Li, H.-L. Yip, Z. Xiao, B. Zhang, Q. Bian, Y. Cheng, S. Liu, M. Cheng, Z. Jin, S. Yang, and L. Ding, "Progress of the key materials for organic solar cells," Sci. China Chem. **63**, 758–765 (2020).
18. K. Nakano, Y. Chen, B. Xiao, W. Han, J. Huang, H. Yoshida, E. Zhou, and K. Tajima, "Anatomy of the energetic driving force for charge generation in organic solar cells," Nature Communications **10**, 2520 (2019).

19. Y. Yuan, T. J. Reece, P. Sharma, S. Poddar, S. Ducharme, A. Gruverman, Y. Yang, and J. Huang, "Efficiency enhancement in organic solar cells with ferroelectric polymers," Nature Materials **10**, 296–302 (2011).
20. K. Wang, C. Liu, T. Meng, C. Yi, and X. Gong, "Inverted organic photovoltaic cells," Chem. Soc. Rev. **45**, 2937–2975 (2016).
21. M. S. Alias, S. A. Kamaruddin, N. Nafarizal, and M. Z. Sahdan, "Performance of inverted organic solar cell using different metal electrodes," in *2014 IEEE International Conference on Semiconductor Electronics (ICSE2014)* (2014), pp. 416–419.
22. J. D. Servaites, M. A. Ratner, and T. J. Marks, "Organic solar cells: A new look at traditional models," Energy & Environmental Science **4**, 4410–4422 (2011).
23. C. L. Chochos, M. Spanos, A. Katsouras, E. Tatsi, S. Drakopoulou, V. G. Gregoriou, and A. Avgeropoulos, "Current status, challenges and future outlook of high performance polymer semiconductors for organic photovoltaics modules," Progress in Polymer Science **91**, 51–79 (2019).
24. N. Li, I. McCulloch, and C. J. Brabec, "Analyzing the efficiency, stability and cost potential for fullerene-free organic photovoltaics in one figure of merit," Energy & Environmental Science **11**, 1355–1361 (2018).
25. A. Anctil, C. W. Babbitt, R. P. Raffaelle, and B. J. Landi, "Material and Energy Intensity of Fullerene Production," Environ. Sci. Technol. **45**, 2353–2359 (2011).
26. T. M. Grant, K. L. C. Kaller, T. J. Coathup, N. A. Rice, K. Hinzer, and B. H. Lessard, "High Voc solution-processed organic solar cells containing silicon phthalocyanine as a non-fullerene electron acceptor," Organic Electronics **87**, 105976 (2020).
27. M.-T. Dang, T. M. Grant, H. Yan, D. S. Seferos, B. H. Lessard, and T. P. Bender, "Bis(tri-n-alkylsilyl oxide) silicon phthalocyanines: a start to establishing a structure property relationship as both ternary additives and non-fullerene electron acceptors in bulk heterojunction organic photovoltaic devices," J. Mater. Chem. A **5**, 12168–12182 (2017).
28. T. Nyokong, "Effects of substituents on the photochemical and photophysical properties of main group metal phthalocyanines," Coordination Chemistry Reviews **251**, 1707–1722 (2007).
29. S. Honda, T. Nogami, H. Ohkita, H. Benten, and S. Ito, "Improvement of the light-harvesting efficiency in polymer/fullerene bulk heterojunction solar cells by interfacial dye modification," ACS Appl Mater Interfaces **1**, 804–810 (2009).
30. E. Zysman-Colman, S. S. Ghosh, G. Xie, S. Varghese, M. Chowdhury, N. Sharma, D. B. Cordes, A. M. Z. Slawin, and I. D. W. Samuel, "Solution-Processable Silicon Phthalocyanines in Electroluminescent and Photovoltaic Devices," ACS Appl. Mater. Interfaces **8**, 9247–9253 (2016).
31. H. Jiang, P. Hu, J. Ye, R. Ganguly, Y. Li, Y. Long, D. Fichou, W. Hu, and C. Kloc, "Hole Mobility Modulation in Single-Crystal Metal Phthalocyanines by Changing the Metal–π/π–π Interactions," Angewandte Chemie **130**, 10269–10274 (2018).
32. G. Löbbert, "Phthalocyanines," in *Ullmann's Encyclopedia of Industrial Chemistry* (American Cancer Society, 2000).
33. M. K. Lowery, A. J. Starshak, J. N. Esposito, P. C. Krueger, and M. E. Kenney, "Dichloro(phthalocyanino)silicon," Inorg. Chem. **4**, 128–128 (1965).
34. T. Gessner, R. Sens, W. Ahlers, and C. Vamvakaris, "Preparation of silicon phthalocyanines and germanium phthalocyanines and related substances," United States patent US20100113767A1 (May 6, 2010).
35. A. Anctil, C. W. Babbitt, R. P. Raffaelle, and B. J. Landi, "Cumulative energy demand for small molecule and polymer photovoltaics," Progress in Photovoltaics: Research and Applications **21**, 1541–1554 (2013).
36. W. Zhao, S. Li, H. Yao, S. Zhang, Y. Zhang, B. Yang, and J. Hou, "Molecular Optimization Enables over 13% Efficiency in Organic Solar Cells," J. Am. Chem. Soc. **139**, 7148–7151 (2017).

37. A. Hemani, D. Benmoussa, A. NOURI, H. Khachab, and B. Dekkich, "Effect of the FSF and BSF layers on the performances of the GaAS solar cell," Journal of Ovonic Research **13**, 307–314 (2017).
38. C. E. Valdivia, M. M. Wilkins, S. S. Chahal, F. Proulx, P.-O. Provost, D. P. Masson, S. Fafard, and K. Hinzer, "Many-junction photovoltaic device performance under non-uniform high-concentration illumination," AIP Conference Proceedings **1881**, 070005 (2017).
39. S. Fafard, "New and Future III-V Cells and Concepts," in *Photovoltaic Solar Energy* (John Wiley & Sons, Ltd, 2016), pp. 383–395.
40. S. Hubbard, "Absorption and Generation," in *Photovoltaic Solar Energy* (John Wiley & Sons, Ltd, 2016), pp. 32–38.
41. D. Xia, M. N. Beattie, M. C. Tam, M. M. Wilkins, C. E. Valdivia, Z. R. Wasilewski, K. Hinzer, and J. J. Krich, "Detailed Balance Efficiency of 1310 nm Multijunction Photonic Power Converters," in *2019 International Conference on Numerical Simulation of Optoelectronic Devices (NUSOD)* (2019), pp. 69–70.
42. I. Vurgaftman, J. R. Meyer, and L. R. Ram-Mohan, "Band parameters for III–V compound semiconductors and their alloys," Journal of Applied Physics **89**, 5815–5875 (2001).
43. M. Levinshtein, S. Rumyantsev, and M. Shur, *Handbook Series on Semiconductor Parameters: Volume 2: Ternary And Quaternary III-V Compounds* (WORLD SCIENTIFIC, 1996), Vol. 2.
44. M. Sotoodeh, A. H. Khalid, and A. A. Rezazadeh, "Empirical low-field mobility model for III–V compounds applicable in device simulation codes," Journal of Applied Physics **87**, 2890–2900 (2000).
45. "Optical Data from Sopra SA," http://www.sspectra.com/sopra.html.
46. S. J. Byrnes, "Multilayer optical calculations," arXiv preprint arXiv:1603.02720 (2016).
47. Adrian Kitai, *Principles of Solar Cells, LEDs and Diodes: The Role of the PN Junction* (John Wiley & Sons, Ltd, 2011).
48. HORIBA Jobin Yvon, "Cauchy and related Empirical Dispersion Formulae for Transparent Materials," (n.d.).
49. HORIBA Jobin Yvon, "New Amorphous Dispersion Formula," (n.d.).
50. C. Stelling, C. R. Singh, M. Karg, T. A. F. König, M. Thelakkat, and M. Retsch, "Plasmonic nanomeshes: their ambivalent role as transparent electrodes in organic solar cells," Scientific Reports **7**, 42530 (2017).
51. M. T. Dang, L. Hirsch, and G. Wantz, "P3HT:PCBM, Best Seller in Polymer Photovoltaic Research," Advanced Materials **23**, 3597–3602 (2011).
52. D. Qian, L. Ye, M. Zhang, Y. Liang, L. Li, Y. Huang, X. Guo, S. Zhang, Z. Tan, and J. Hou, "Design, Application, and Morphology Study of a New Photovoltaic Polymer with Strong Aggregation in Solution State," Macromolecules **45**, 9611–9617 (2012).
53. B. Kadem, A. Hassan, and W. Cranton, "Efficient P3HT:PCBM bulk heterojunction organic solar cells; effect of post deposition thermal treatment," J Mater Sci: Mater Electron **27**, 7038–7048 (2016).
54. B. Kadem, W. Cranton, and A. Hassan, "Metal salt modified PEDOT:PSS as anode buffer layer and its effect on power conversion efficiency of organic solar cells," Organic Electronics **24**, 73–79 (2015).
55. J. Müllerová, M. Kaiser, V. Nádaždy, P. Šiffalovič, and E. Majková, "Optical absorption study of P3HT:PCBM blend photo-oxidation for bulk heterojunction solar cells," Solar Energy **134**, 294–301 (2016).
56. Z. Zheng, H. Yao, L. Ye, Y. Xu, S. Zhang, and J. Hou, "PBDB-T and its derivatives: A family of polymer donors enables over 17% efficiency in organic photovoltaics," Materials Today **35**, 115–130 (2020).

57. M. P. Aplan, J. M. Munro, Y. Lee, A. N. Brigeman, C. Grieco, Q. Wang, N. C. Giebink, I. Dabo, J. B. Asbury, and E. D. Gomez, "Revealing the Importance of Energetic and Entropic Contributions to the Driving Force for Charge Photogeneration," ACS Appl. Mater. Interfaces **10**, 39933–39941 (2018).
58. N. A. Ran, J. A. Love, M. C. Heiber, X. Jiao, M. P. Hughes, A. Karki, M. Wang, V. V. Brus, H. Wang, D. Neher, H. Ade, G. C. Bazan, and T.-Q. Nguyen, "Charge Generation and Recombination in an Organic Solar Cell with Low Energetic Offsets," Advanced Energy Materials **8**, 1701073 (2018).
59. L. J. A. Koster, V. D. Mihailetchi, H. Xie, and P. W. M. Blom, "Origin of the light intensity dependence of the short-circuit current of polymer/fullerene solar cells," Appl. Phys. Lett. **87**, 203502 (2005).
60. P. Kumar, S. C. Jain, H. Kumar, S. Chand, and V. Kumar, "Effect of illumination intensity and temperature on open circuit voltage in organic solar cells," Appl. Phys. Lett. **94**, 183505 (2009).
61. J. A. Barker, C. M. Ramsdale, and N. C. Greenham, "Modeling the current-voltage characteristics of bilayer polymer photovoltaic devices," Phys. Rev. B **67**, 075205 (2003).
62. C. M. Proctor and T.-Q. Nguyen, "Effect of leakage current and shunt resistance on the light intensity dependence of organic solar cells," Appl. Phys. Lett. **106**, 083301 (2015).
63. M. M. Mandoc, F. B. Kooistra, J. C. Hummelen, B. de Boer, and P. W. M. Blom, "Effect of traps on the performance of bulk heterojunction organic solar cells," Appl. Phys. Lett. **91**, 263505 (2007).
64. A. Sharma, M. Chauhan, V. Bharti, M. Kumar, S. Chand, B. Tripathi, and J. P. Tiwari, "Revealing the correlation between charge carrier recombination and extraction in an organic solar cell under varying illumination intensity," Physical Chemistry Chemical Physics **19**, 26169–26178 (2017).
65. G. Dennler, K. Forberich, M. C. Scharber, C. J. Brabec, I. Tomiš, K. Hingerl, and T. Fromherz, "Angle dependence of external and internal quantum efficiencies in bulk-heterojunction organic solar cells," Journal of Applied Physics **102**, 054516 (2007).
66. M. Wilkins, C. E. Valdivia, S. Chahal, M. Ishigaki, D. P. Masson, S. Fafard, and K. Hinzer, "Performance impact of luminescent coupling on monolithic 12-junction phototransducers for 12 V photonic power systems," in *Physics, Simulation, and Photonic Engineering of Photovoltaic Devices V* (International Society for Optics and Photonics, 2016), Vol. 9743, p. 97430W.
67. M. N. Beattie, Zamiri, M., Kaller, K.L.C., Wilkins, M.M., Valdivia, C.E., Xia, D., Tam, M.C., Kim, H., Krich, J.J., Wasilewski, Z., and Hinzer, K., "Two-junction III-V photonic power converter operating at monochromatic telecom wavelengths," in *2020 IEEE 47th Photovoltaic Specialists Conference* (June 14-19).
68. Zamiri, M., Nouri, N., Kaller, K.L.C., Beattie, M.N., Wilkins, M.M., Valdivia, C.E., Lessard, B., Wasilewski, Z.R., and Hinzer, K., "Design for fabrication of high efficiency 1310 nm photonic power converter," in *19th International Conference on Numerical Simulation of Optoelectronic Devices* (July 8-12).
69. M. N. Beattie, C. E. Valdivia, M. M. Wilkins, M. Zamiri, K. L. C. Kaller, M. C. Tam, H. S. Kim, J. J. Krich, Z. R. Wasilewski, and K. Hinzer, "High current density tunnel diodes for multi-junction photovoltaic devices on InP substrates," Appl. Phys. Lett. **118**, 062101 (2021).
70. P. Huo, B. Galiana, and I. Rey-Stolle, "Comparison of Ti/Pd/Ag, Pd/Ti/Pd/Ag and Pd/Ge/Ti/Pd/Ag contacts to n-type GaAs for electronic devices handling high current densities," Semicond. Sci. Technol. **32**, 045006 (2017).
71. E. F. Chor, D. Zhang, H. Gong, W. K. Chong, and S. Y. Ong, "Electrical characterization, metallurgical investigation, and thermal stability studies of (Pd, Ti, Au)-based ohmic contacts," Journal of Applied Physics **87**, 2437–2444 (2000).
72. D. G. Ivey, P. Jian, L. Wan, R. Bruce, S. Eicher, and C. Blaauw, "Pd/Zn/Pd/Au ohmic contacts to ρ-Type InP," JEM **20**, 237–246 (1991).

73. O. Salehzadeh, G. Bonneville, O. J. Pitts, and A. J. Springthorpe, "Edge Breakdown Suppression of Avalanche Photodiodes Using Zn Diffusion and Selective Area Growth," IEEE Photonics Technology Letters **31**, 767–770 (2019).
74. M. Tong, K. Nummila, A. A. Ketterson, I. Adesida, L. Aina, and M. Mattingly, "Selective Wet Etching Characteristics of Lattice-Matched InGaAs / InAlAs / InP," J. Electrochem. Soc. **139**, L91 (1992).
75. M. F. Bennett, M. González, M. P. Lumb, M. K. Yakes, K. J. Schmieder, S. Tomasulo, J. Abell, J. R. Meyer, and R. J. Walters, "Development of wet etch processing for InxAl1−xAsySb1−y solar cells grown on InP," in *2015 IEEE 42nd Photovoltaic Specialist Conference (PVSC)* (2015), pp. 1–4.
76. Kaller, K.L.C., Valdivia, C.E., Lessard, B., and Hinzer, K., "Design and modelling of photonic power converters with light management in Solcore," in *19th International Conference on Numerical Simulation of Optoelectronic Devices* (19th International Conference on Numerical Simulation of Optoelectronic Devices, 2019).